N O T I C E

THIS DOCUMENT HAS BEEN REPRODUCED FROM MICROFICHE. ALTHOUGH IT IS RECOGNIZED THAT CERTAIN PORTIONS ARE ILLEGIBLE, IT IS BEING RELEASED IN THE INTEREST OF MAKING AVAILABLE AS MUCH INFORMATION AS POSSIBLE
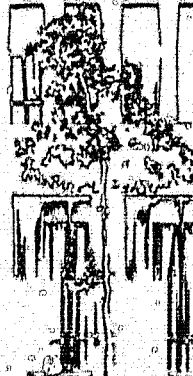
(NASA-CR-162038) THE PHORETIC MOTION
EXPERIMENT (PME) DEFINITION PHASE Final
Report (TRW Defense and Space Systems Group)
100 p HC A05/MF A01   CSCL 14B

N82-27329

Unclas
G3/14   28253

May 14, 1982

THE PHORETIC MOTION EXPERIMENT (PME)

DEFINITION PHASE

FINAL REPORT

PREPARED FOR

George C. Marshall Space Flight Center
Marshall Space Flight Center
Alabama 35812

Under Contract No. NAS 8-34319

PREPARED BY:

L. R. Eaton   TRW
S. L. Neste   GE

TRW

DEFENSE AND SPACE SYSTEMS GROUP

ACKNOWLEDGEMENTS

ABSTRACT

This report has emphasized analysis of the aerosol generator and the CFD chamber which were designed for zero-gravity operation under a NASA ACPL program contract. These analysis were started as part of a PME (Phoretic Motion Activity) contract (NAS 8-33149) with Dr. Larry Eaton as principle investigator and Dr. Sherman Neste as co-principle investigator. The initial results were summarized in a final report to NASA in September, 1981 (NASA/MSFC).

These above results have been expanded during the NAS 8-34319 contract activity by Dr. Eaton. The primary objective of the effort has been to document, characteristics of the CFD chamber and aerosol generator which would be useful for cloud physics experimentation in a one-g as well as a zero-g environment. The delineation of these characteristics were required for the PME shuttle experiment but funding constraints has not permitted the results to be extended to the specific PME requirements.

Part A of this final report addresses the Collison type of aerosol generator. Relationships amoung the various input and output parameters are derived and subsequently used to determine the requirements on the controls of the input parameters to assure a given error budget of an output parameter. this parameterization should be useful in all areas of terrestrial research and industry where these types of aerosol atomizers are used.

Part B assesses the CFD chamber operation in a zero-g environment utilizing a computer simulation program which had been developed by Dr. M Plooster for the ACPL program. Low nuclei critical supersaturation and high experiment accuracies are emphasized which lead to droplet growth times extending into hundreds of seconds. It is these long droplet growth times which require a low accelleration operating environment for the CFD chamber. The analysis has been extended to assess the performance constraints of the CFD chamber in a one-g environment operating in the horizontal mode.

CONTENTS
PART A
AEROSOL GENERATOR

CONTENTS
PART B
CFD CHAMBER

ILLUSTRATIONS
PART A
AEROSOL GENERATOR

v

ILLUSTRATIONS
PART B
CFD CHAMBER

PART A

ZERO-G AEROSOL GENERATOR

I. INTRODUCTION

Atomizers have been built for such diverse purposes as aerosolization of samples for spectroscopic analysis, medication via inhalation and cloud generation for atmospheric research. In many of the research and analytical applications, aerosol production stability and repeatability are key desired attributes. Although a wide variety of atomizer designs exist, there is still a severe lack of quantitative information which relates the physical and operating parameters to the atomizer's output, be it particle size distribution or mass concentration.

The results reported herein evolved from the need for an atomizer to produce submicron aerosols which had the fundamental characteristics of high stability and repeatability ($\pm$ 2% rms in 15 min., $\pm$ 4% rms in 45 min. and $\pm$ 5% rms day to day). These attributes were also to be compatible with the additional stringent requirements of: operating in a low acceleration environment ($<< 10^{-3}$ of the earth's gravitational field); highly automated to provide hands-off operation under computer control; high reliability due to inaccessability driven by the need for time efficiency in an awkward working environment, and an operating time in excess of a hundred hours over a period of a week. The unit also had to operate after being in a waiting mode for several months and after surviving a Shuttle launch. Although some of these requirements are not necessary for terrestrial applications, the resulting generator design remair simple enough that beneficial use can be made of many of these design features. For example, the zero-g operation capability permits utilization of the generator in any desired orientation in a terrestrial laboratory.

As the generator was being tested and characterized, it became apparent that empirical relationships between the input and output parameters of the generator would greatly enhance the optimization of the design as well as permit modelling of the generator performance for use in correlating experiment requirements with operational parameters. These relationships are also very useful in assessing parameter sensitivity and hence in defining the precision to which these parameters must be controlled, particularly the fluid flow and air pressure.

The following sections give an overview of the generator design and list some of the data collected, but the main emphasis is placed on the empirical relationships among the primary operating parameters.

II. GENERATOR DESIGN

The specific application which motivated the generator design, was to provide an aerosol of NaCl particles with a geometric mean diameter of around 0.04 μm. In addition, the generator was required to provide an aerosol of high stability and to operate unattended for long periods of time as mentioned previously. A literature review indicated that the Collison type of atomizer using a volatile solvent (water) was the most promising concept. Specifically, the TSI Inc. constant output atomizer (COA) with non-recycled fluid formed the foundation for the new generator development activity. The basic COA head geometry was retained (Figure 1) with the primary development activity being directed toward the requirement of performing in a zero-gravity (low acceleration) environment with enhanced aerosol generator stability and repeatability.

At the outset, the TSI supplied syringe pump was found to have unacceptable fluid delivery rate fluctuations as well as limited operating time before handling was required. The extended operating time, containment of excess fluid in zero-g and overall stability improvement were accomplished by the following design changes: a sapphire orifice (Bird Precision Jewel, Waltham, MA) was used to eliminate orifice irregularities and erosion; the exit face (except the exit channel itself) of the atomizer was covered with a fine mesh wicking screen to eliminate fluid accumulation points; the complete impaction area and the reservoir for excess fluid was packed with a very high purity quartz fiber wicking material (Q-Fisher quartz felt, John's Manville) to absorb excess fluid; a high precision, low leakage, valveless fluid pump (RHOCKC, Fluid Metering Inc., Oyster Bay, NY) supplied degassed fluid from a collapsible low gas permeable bag (Teflon or Tedlar); and a well regulated air

3

AEROSOL
OUT

0.0135 DIA (NO. 80 DRILL)
HOLE IN ⁷/8 DIA DISC

COMPRESSED AIR IN ⟶

"O"-RING

LIQUID
IN

EXCESS
LIQUID
TO CLOSED
RESERVOIR
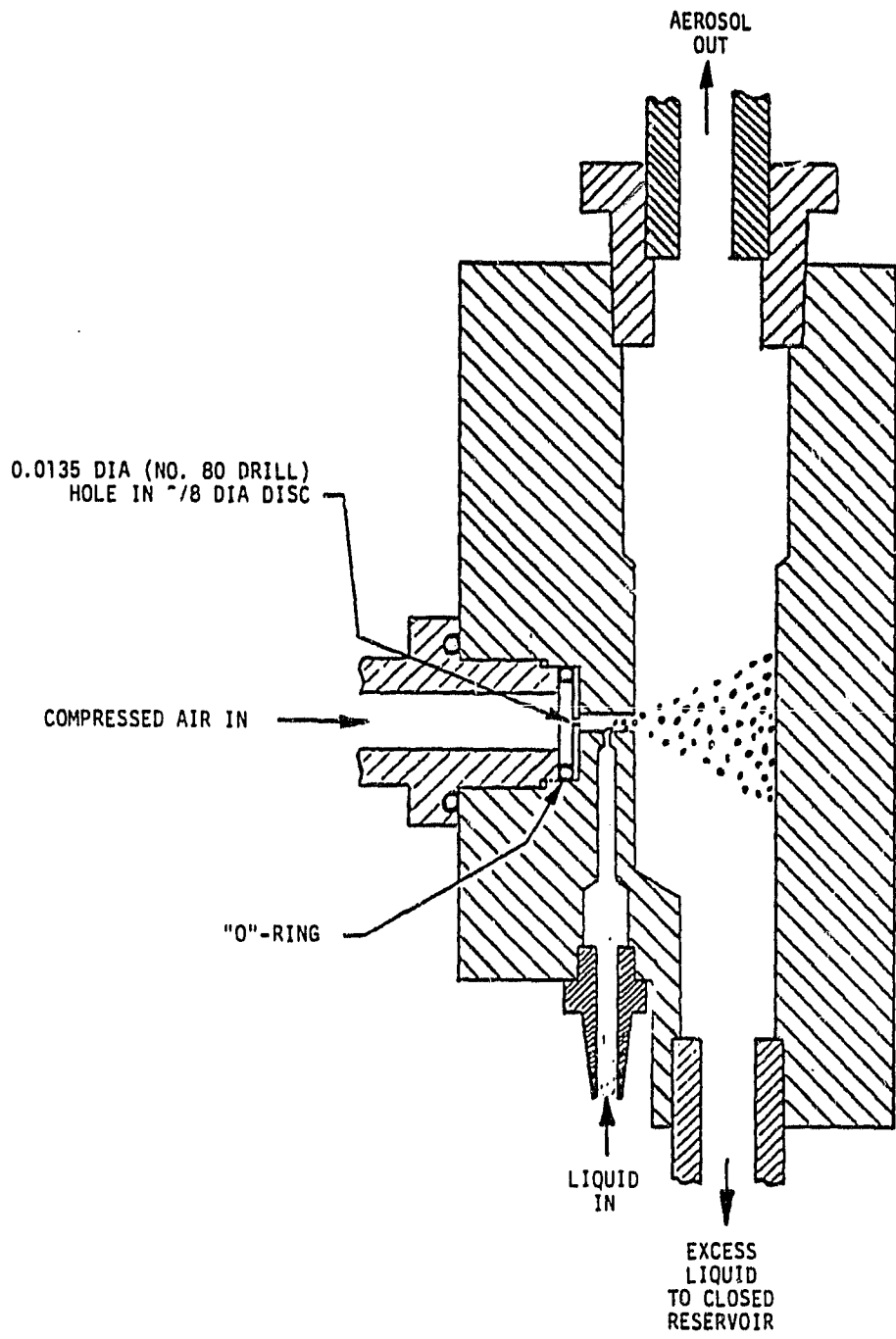
Figure 1.   COA (TSI) Atomizer Assembly

supply from a diaphram air pump provided precisely controlled, filtered air. A sketch of the NASA ACPL flight version of the atomizer assembly is given in Figure 2. Some parts of this zero-g design are discussed in later sections.

Laboratory measurements were made to characterize the atomizer output for a range of values of the fluid delivery rate and air pressure to the atomizer head. The laboratory test configuration including the automatic control and data acquisition system as depicted in Figure 3 was used to evaluate the hands-off operation of the aerosol generation, manipulation and measurement systems as well as to provide the data to characterize the generator. Manual readings from electronic balances were also made to determine the fluid delivery rate to the atomizer (Mettler PC 4400) and the excess fluid accumulation rate within the wicked reservoir (Mettler P5). These latter measurements were used to obtain absolute fluid delivery rates and atomizer efficiencies. The estimated measurement accuracies and the basic data are given in Table 1 and 2, respectively.
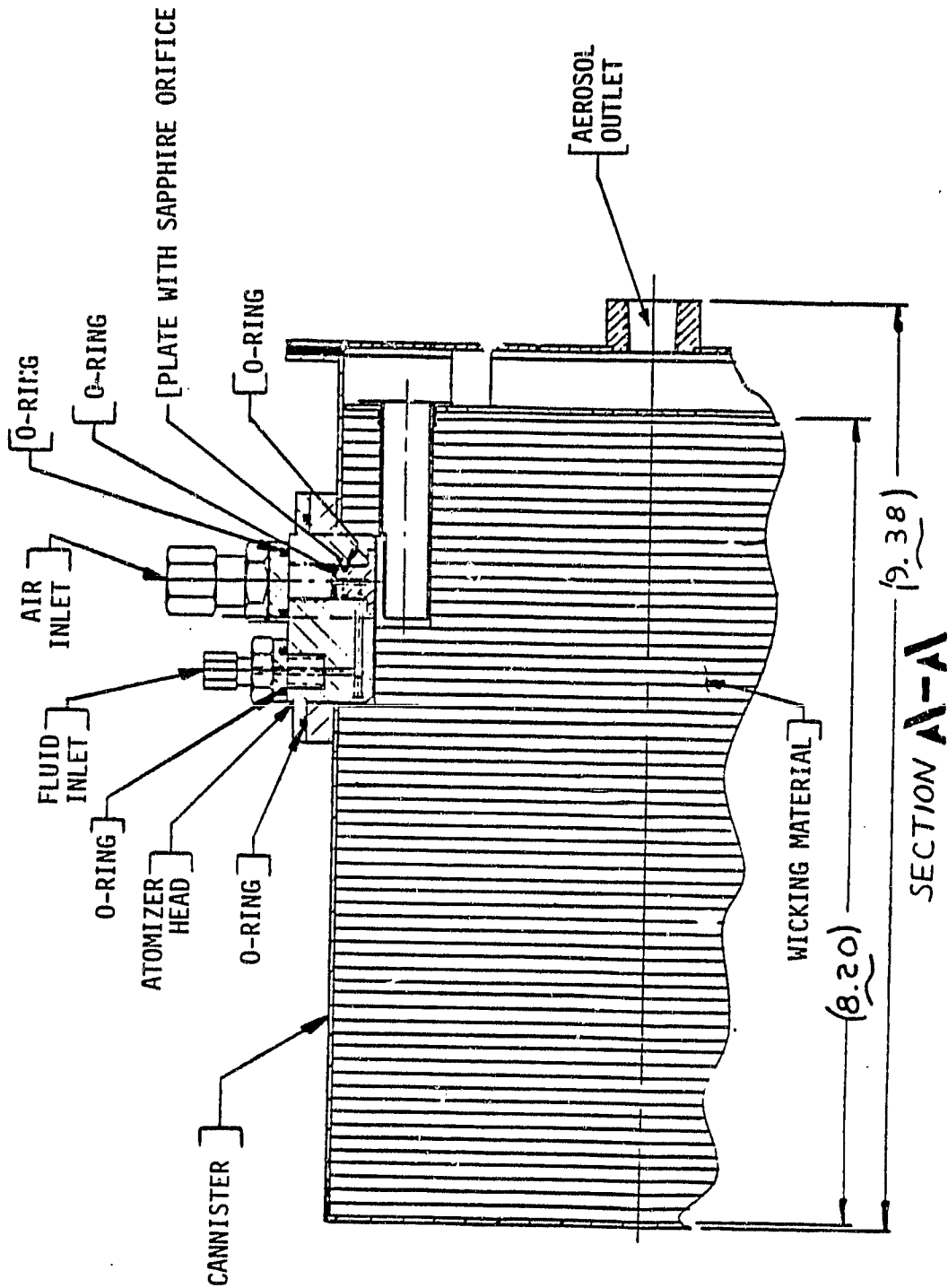
Figure 2. ACPL Zero-G Atomizer Assembly

6

FM - Flowmeter
F - Filter
EC - Electrostatic Classifier
EAD - Electrical Aerosol Detector
EAA - Electrical Aerosol Analyser
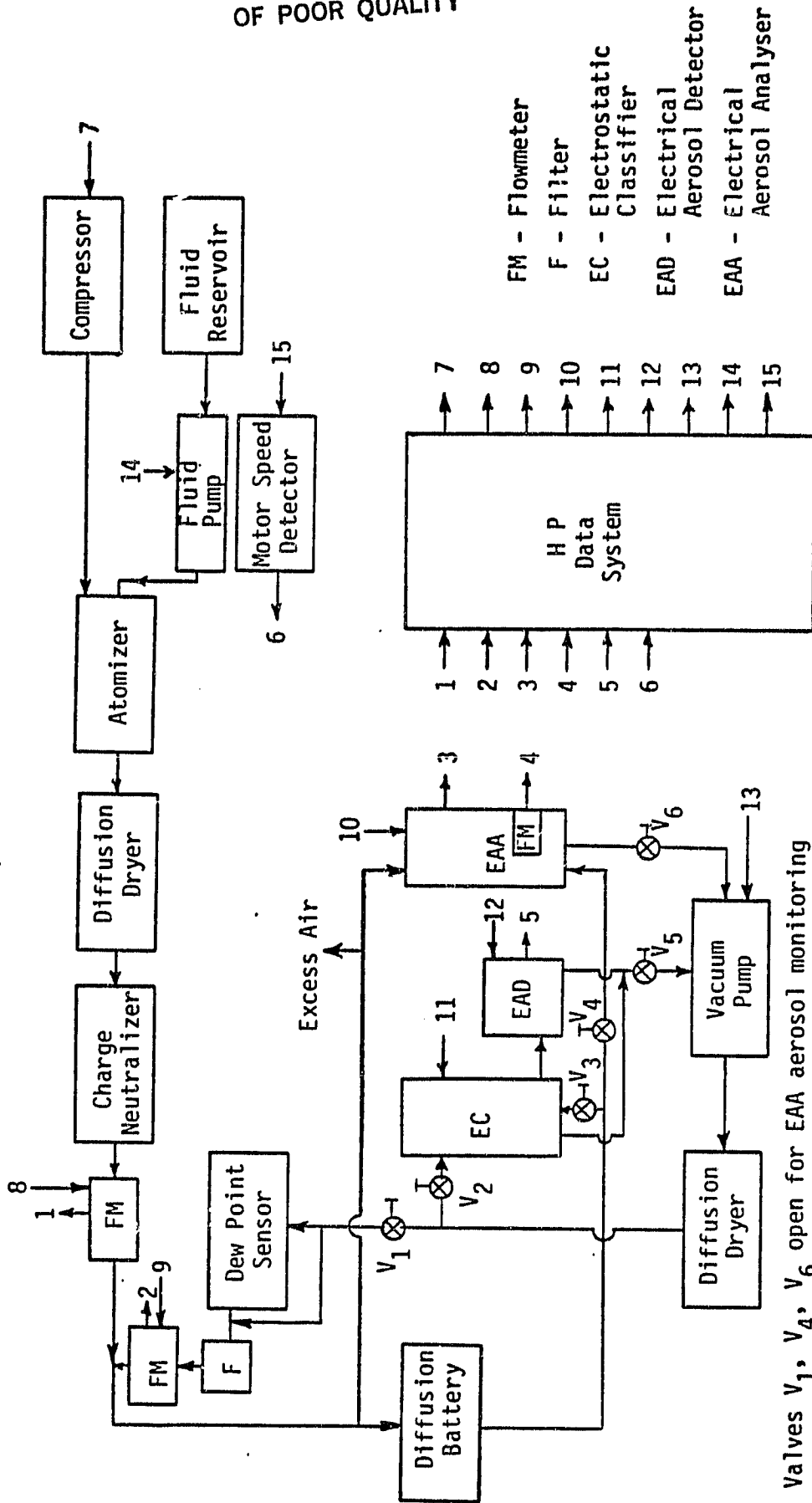
1- 6 Data Outputs Monitored
7-15 Control Commands Sent

Valves V_1, V_4, V_6 open for EAA aerosol monitoring
Valves V_2, V_3, V_5 open for EC/EAD aerosol monitoring

Figure 3. Aerosol Laboratory Test Configuration

7

TABLE 1. Experimental Measurement Error Estimates

Apparatus	Accuracy	Resolution
TSI Model 2011 Electronic Flowmeters	±2% of reading	±0.5% of reading
Mettler PC4400 Electronic Balance	±0.003 gm	±0.001 gm
Mettler P5 Electronic Balance	±0.05 gm	±0.01 gm
TSI Electrical Aerosol Size Analyzer	±0.003 V	±0.001 V
Fairchild Pressure Gauge	±0.5 PSI	±0.2 PSI

TABLE 2. ACPL Atomizer Data

ΔP (PSI)	$\dot{q}$ ($\mu l/sec$)	E (%)	$\dot{Q}$ (l/sec)	C ($\mu l/l$)	N (No./cc$\times 10^6$)	$\dot{q}''$ ($\mu l/sec$)	d_g (μm)	σ_g	d_m (μm)
15	0.595	79.20	0.0348	13.54	0.557	0.471	0.0298	2.433	0.0976
15	1.625	30.09	0.0348	14.04	0.945	0.489	0.0368	2.261	0.0998
15	5.178	8.51	0.0345	12.43	1.536	0.441	0.0424	2.289	0.1186
15	8.612	6.45	0.0355	15.64	1.839	0.555	0.0417	2.178	0.1036
15	11.982	4.73	0.0354	16.00	2.149	0.567	0.0412	2.109	0.1059
15	15.818	3.59	0.0358	15.87	2.337	0.568	0.0489	2.094	0.1109
15	20.050	3.02	0.0357	16.94	2.401	0.606	0.0465	2.123	0.1089
25	0.635	92.88	0.0475	12.41	0.833	0.590	0.0327	2.318	0.0943
25	0.835	71.64	0.0470	12.72	0.896	0.582	0.0318	2.326	0.0926
25	1.748	36.69	0.0470	13.64	1.610	0.641	0.0361	2.235	0.0952
25	5.097	12.21	0.0469	13.25	2.458	0.622	0.0424	2.133	0.1003
25	5.200	12.56	0.0468	13.94	2.699	0.653	0.0425	2.11	0.1005
25	8.650	8.79	0.0470	16.17	3.305	0.760	0.0423	2.145	0.1016
25	11.933	6.01	0.0475	15.10	3.998	0.717	0.0530	2.005	0.1096
25	15.917	4.95	0.0476	16.55	4.300	0.788	0.0514	2.038	0.110
25	19.93	3.90	0.0476	16.34	4.432	0.777	–	–	–
35	0.805	93.45	0.0595	12.64	0.957	0.752	0.0348	2.236	0.0918
35	1.868	40.92	0.0595	12.85	1.856	0.764	–	–	–
35	5.192	15.31	0.0605	13.14	3.432	0.795	0.0368	2.213	0.0947
35	8.607	10.63	0.0597	15.33	4.386	0.915	0.0489	2.055	0.1065
35	11.952	7.62	0.0603	15.11	5.193	0.911	0.0490	2.038	0.1047
35	15.833	5.64	0.0599	14.90	5.695	0.893	0.0495	2.037	0.1057
35	20.037	5.18	0.0601	17.28	6.126	1.04	–	–	–

III. ANALYTICAL/EMPIRICAL RELATIONSHIPS

The primary operationally controlled parameters of the Collison type of atomization process are the fluid delivery rate and the differential air pressure applied across the generator orifice. Figure 4 depicts these input parameters along with a number of output parameters. The parameter units and how they were obtained as applicable to the present paper are also given. Items 1, 2, 3, 4 and 9 were measured while the rest were derived from these five measurements. Existing and analytically derived relationships were used to relate the input and output quantities where possible, with empirically derived relationships being used when necessary.

1. Absolute Pressure - P_o (Item 1, Figure 4)

    A diaphram pump, dual stage pressure regulator, air drier and a particle filter (99.99% efficient at 0.3 μm) provided the precisely controlled dry air supply for the generator. Regulation stability, dryness and cleanliness of the air supply are all important factors which are often overlooked. The gauge pressure was measured (i.e., pressure above ambient) giving the delta pressure ΔP, across the orifice since the down stream side of the orifice was at ambient pressure P_a (within the gauge accuracy), hence $P_o = \Delta P + P_a$.

    The three values of 1, 1.67 and 2.33 atm (15, 25 and 35 PSI) were selected for P as summarized in the left column of Table 2. The pressures were selected to keep the orifice flow in the sonic or chocked flow regime. The scope of the test program did not permit the subsonic regime to be characterized.

9

	Parameter	Description	Units		
←	P_o	Absolute Pressure	Atmospheres	1.	Measured
GEN ←	$\dot{q}$	Fluid Delivery Rate	$\mu\ell/sec$	2.	Measured
→	$\dot{q}'$	Non-Atomized Fluid	$\mu\ell/sec$	3.	Measured
	P_a	Ambient Pressure	Atmospheres	4.	Measured
	$\dot{Q}$	Air Flow Rate $\dot{Q}(\Delta p = p_o - p_a) = f(p_a + \Delta p) = a(p_a + \Delta p)$	ℓ/sec	5.	Calculated (Measured initially for calibration)
	$\dot{q}''$	Mass Atomized $\dot{q}'' = E\dot{q} = \dot{q} - \dot{q}'$	$\mu\ell/sec$	6.	Calculated From 2&3
	E	Atomization Efficiency $E = (\dot{q} - \dot{q}')/\dot{q}$	Fractional	7.	Calculated From 6
	C	Concentration of Water in Unit Volume of Air $C = \dot{q}''/\dot{Q}$	$\mu\ell/\ell$	8.	Theory (Computed) + Data
	N	Aerosol Concentration Distribution	$No./\mu$	9.	Measured
	$\bar{d}$	Mean Droplet Diameter	μm	10.	Computed Using 9
	σ_d	Standard Deviation	μm	11.	Computed Using 9

Figure 4. Fluids Parameters

2. Fluid Delivery Rate - $\dot{q}$ (Item 2, Figure 4)

Special care was taken to provide a fluid flow rate whose time average over a few seconds was very stable. Prevention of air bubble formation was an important aspect as well as keeping the fluid supply entrance diameter as small as practical. Several types of flow meters were tried for the low fluid flow rates required, but were found to be unsatisfactory, so a precision electronic balance was used to measure the rate of weight decrease of the fluid supply reservoir. This procedure resulted in the delivery rates given in Column 2 of Table 2 which are rates averaged over a few minutes, the exact time being dependent on actual flow rates (1% readings were sought). An indication of the second to second stability of the overall generation/aerosol-handling process was given by the faster responding aerosol concentration (N) measurement equipment. Figure 5 indicates the improved stability performance provided by the change in fluid pumps.

3. Non-Atomized Fluid - $\dot{q}'$ (Item 3, Figure 4)

The quantity $\dot{q}'$ is that portion of the delivered fluid which does not exit the generator as useful aerosol. It consists of the fluid which is forced out of the generator head in bulk and of the larger droplets which impact and remain attached to the impaction surface. The excess fluid reservoir was weighed on an electronic balance in a similar fashion as the fluid supply. Due to the much larger reservoir mass, a larger balance with lower mass resolution was required which resulted in mass accumulation rates averaged over a

11
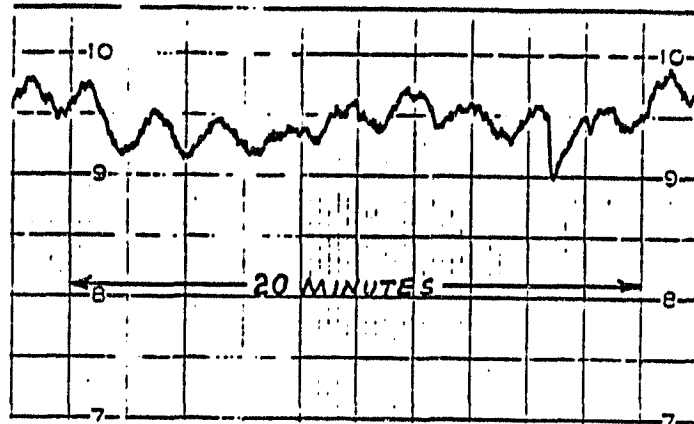
Aerosol Output Using Harvard Apparatus Syringe Pump
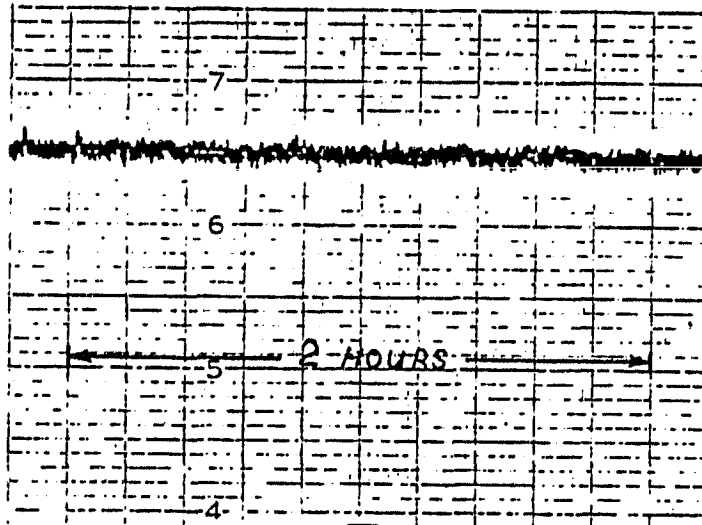
Aerosol Output Using FMI Fluid Pump

Figure 5. Aerosol Generation Stability-Analog Data

time approximately ten times the fluid delivery rates. These measurements were combined with the fluid delivery rates and are contained within the efficiency numbers, E, of Table 2 (c.f. Item 7 below).

4. Ambient Pressure - P_a (Item 4, Figure 4)

The aerosol exits from the generator at ambient pressure to within the ΔP pressure measurement accuracy. The laboratory measurements were made near sea level and a rounded nominal value of 15 PSI for P_a sufficed for the present analysis.

5. Air Flow Rate - $\dot{Q}$ (Item 5, Figure 4)

Mercer, et al. (1968) gave a relationship for the air mass flow rate $\dot{Q}$ through an orifice as a function of the orifice cross-section area, a, initial temperature T_0, downstream air pressure P_a and the pressure drop, ΔP, across the orifice. For the present application, $\Delta P \geq P_a$, and the appropriate relationship is given by:

$$(\dot{Q}/c \, a \, P_a) = (2.46 \times 10^4/\sqrt{T_0}) \, (1 + \Delta P/P_a) \, (gm/(cm^2\text{-min-atm}))$$

The coefficient of contraction, c, relates the orifice area to the area of the jet at its vena contracta. For a 0.0343 cm (13.5 mil) diameter orifice and temperature T_0 = 296K, this relationship can be rewritten as:

$$c = \dot{Q}/(1.32(P_a + \Delta P)).$$

Average values of $\dot{Q}$ for each ΔP from Table 2 are summarized in Table 3. The last column of this latter table lists the computed values of the coefficient c. The average value of 0.953 $\pm$ 0.007 for this coefficient of contraction was used for subsequent data analysis. Henceforth, $\dot{Q}$ is given in units of liter/sec by:

TABLE 3. Orifice Coefficient of Contraction - c

ΔP		$\dot{Q}$		$P_a + \Delta P$	c
(PSI)	(atm)	(cc/sec)	(gm/min)	(atm)	-
15	1.0	35.36	2.53	2.0	0.9488
25	1.67	47.23	3.38	2.67	0.9484
35	2.33	59.92	4.29	3.33	0.9615

$$\dot{q}'' = [0.3353 + 0.03565 \, (P_a+\Delta P)^2] + [-0.006526 + 0.006481 \, (P_a+\Delta P)]\dot{q}$$

$$\dot{q}'' = 0.7319 + 0.01507\dot{q}$$

$$\dot{q}'' = 0.5865 + 0.01075\dot{q}$$

$$\dot{q}'' = 0.4795 + 0.00645\dot{q}$$
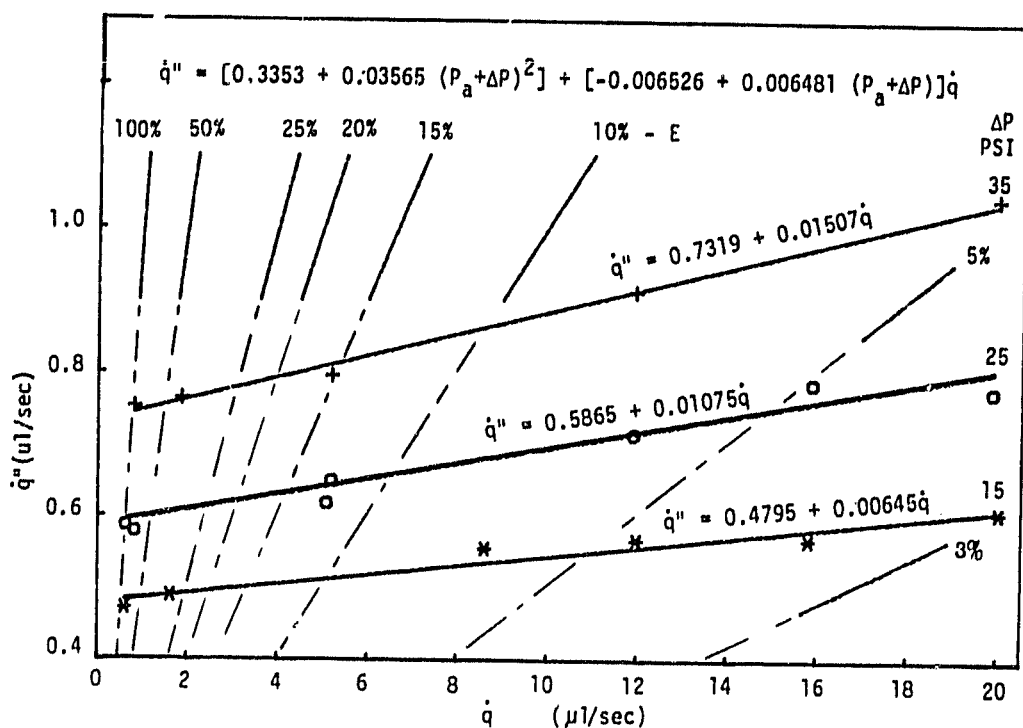
Figure 6. Volume of Atomized Fluid Versus Fluid Delivery Rate

14

$$\dot{Q} = 1.258 \, (P_a + \Delta P) \text{ gm/min}$$

$$= 0.0177 \, (P_a + \Delta P) \text{ l/sec}$$

where dry air $(P_a = 1, \; T_o = 296 \text{ K})$ is assumed for the atomization gas.

6. Volume of Fluid Usefully Atomized - $\dot{q}''$ (Item 6, Figure 4)

    Usefully atomized is defined here as that quantity of fluid which exits the generator as a useable aerosol. The rate of useful atomization (assuming no evaporation) is computed from the difference between the fluid delivery rate and the rate at which the excess fluid accumulates in the wick reservoir, both measured quantities. The values of $\dot{q}''$ from Table 2 are plotted in Figure 6. For a fixed pressure $(P_a + \Delta P)$ the relationship between $\dot{q}''$ and $\dot{q}$ can be approximated by a straight line. The left hand limit of $\dot{q}$ for these straight lines is determined approximately by the line representing $\dot{q}'' = \dot{q}$, that is 100% conversion efficiency. Other atomization efficiency lines for this atomizer are also indicated in this figure. Note that efficiencies up to 100% can be obtained with this type of atomizer with a small sacrifice of output q". Data for fluid delivery rates above 20 µ l/sec was not collected since the high efficiency regime was being emphasized for this particular application (the 10 to 25% region was selected from a trade between atomizer efficiency and particle concentration). A LSQ (least squares) fit was made of each pressure data set with the resulting equations given in Figure 6.

15

The theoretical dependency of these curves on pressure would be difficult to derive since they are not only dependent on increased kinetic energy with higher pressures but also involve a change in the droplet radii spectra. Instead, the coefficients of these individual curve relationships were fitted to various integral powers of the pressure to obtain an approximate pressure dependency. The resulting relationship was:

$$\dot{q}'' = (0.3353+0.03565(P_a+\Delta P)^2+(-0.006526+0.006481(P_a+\Delta P))\dot{q}$$

for the restricted range: $0.6 < \dot{q} < 20 \ \mu l/sec$

$$2 < (P_a + \Delta P) < 3.33 \ atm.$$

For the region below the point where $\dot{q}'' = \dot{q}$, it is expected that $\dot{q}''$ will be equal to $\dot{q}$ down to zero $\dot{q}$ (i.e., moving along the 100% conversion efficiency line indicated in Figure 6).

7. Atomization Efficiency - E (Item 7, Figure 4)

As noted in Figure 4, the flow differences designated by $\dot{q}'' = \dot{q}-\dot{q}'$ is divided by the input fluid flow $\dot{q}$ as supplied by the fluid pump to give the fractional efficiency. The efficiency in percent is thus defined as $E = 100 \ \dot{q}''/\dot{q}$. This is the efficiency of the generator in converting the input fluid supply into useful output aerosol. For most nebulizers which have unrestricted aspirated fluid delivery, this efficiency is usually significantly below one percent. The data in Figure 7 show that the efficiency of the atomization process can be greatly increased by controlling the fluid delivery rate. This efficiency can be as high as 100% but

16
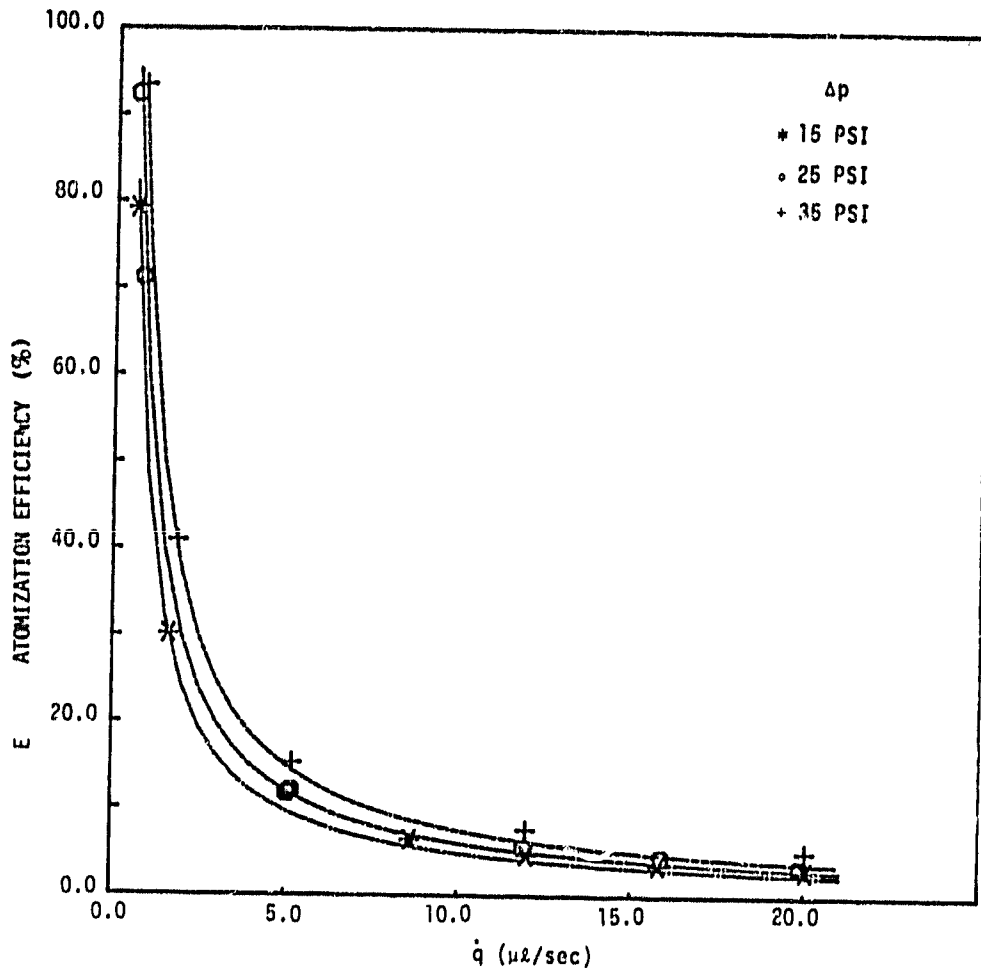
Figure 7. Atomizer Efficiency Versus Fluid Delivery Rate

only with a sacrifice in the total output mass or particle concentration. Optimizing this parameter can be very important in operations such as liquid dispersion for analytical analysis where high accuracy in knowing the quantity delivered (atomized) is important and in other applications where the quantity of precious or hazardous materials used must be minimized.

The form of data in Figure 7 indicates a possible inverse dependency of E on $\dot{q}$. This is confirmed by replotting the data as in Figure 8. The efficiency tends toward 100% as $\dot{q}$ decreases or $\dot{q}^{-1}$ increases. Although flows below 0.6 µl/sec were not assessed, the efficiency should remain a constant 100% below some $\dot{q}$ value and have the displayed $\dot{q}^{-1}$ correlation above this q break point. The relationship between the efficiency, fluid input rate and the pressure is given by:

$$\frac{E(\%)}{100} = \dot{q}''/\dot{q}$$
$$= [-0.006526+0.006481(P_a+\Delta P) + 0.3353+0.3565(P_a + \Delta P)^2]/\dot{q}$$

where the empirically derived relationship for $\dot{q}''$ has been used. Note the expected inverse $\dot{q}$ relationship $E(\%) = a + b/\dot{q}$.

8. Concentration of Water in Air-C (Item 8, Figure 4)

The concentration C is the volume of water (assuming no evaporation) per unit volume of air which has been atomized by the generator and carried away in the air stream. This concentration can be expressed in terms of the measured quantities as $C = \dot{q}''/\dot{Q} = E\dot{q}/\dot{Q}$ giving in terms of measured quantities:

18

$$\frac{E(\%)}{100} = [-0.006526 + 0.006481 \ (P_a + \Delta P)] + [0.3353 + 0.03565 \ (P_a + \Delta P)^2]/\dot{q}$$
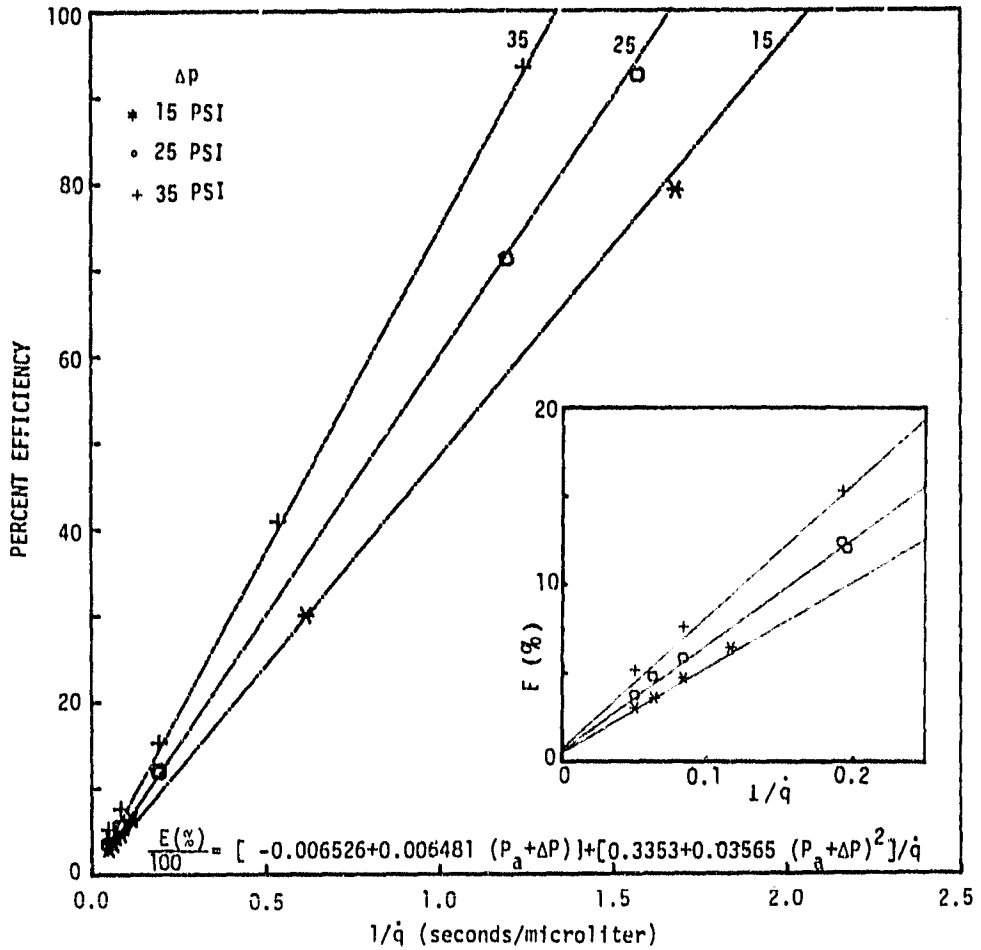
Figure 8.   Efficiency Versus Inverse of Fluid Delivery Rate
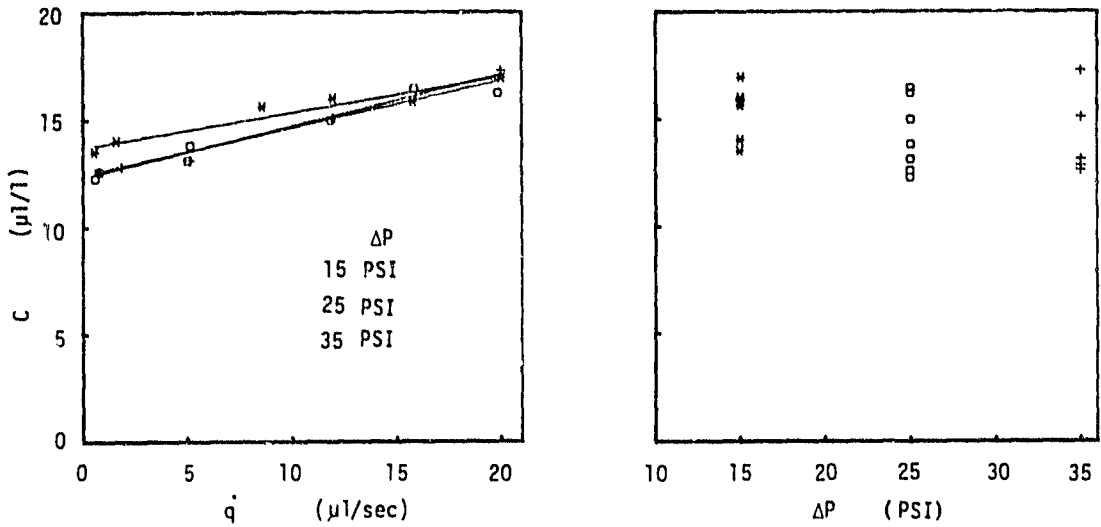
Figure 9.   Mass Concentration of Fluid in Aerosol

19

$$C = (\dot{q} - \dot{q}')/((\text{,} \cup 177(P_a + \Delta P)).$$

Values for C are provided in Table 2. In many medical applications, it is this concentration of fluid carried, e.g., by the inhaled air, that is important.

An examination of the data plotted in Figure 9 shows that for the restricted pressure and fluid flow ranges studied, the concentration has only a small dependency on these parameters.

As the pressure is increased the aerosol output will increase due to the increased conversion efficiency but this factor is countered by the increased air flow which decreases the volume concentration. The equation for $\dot{q}''$ given in the previous section was used in calculating C (c.f., curves in Figure 9) but the result does not show any straightforward pressure dependency as was found with $\dot{q}''$ and E. The various C curves for fixed pressures cross at different points. A LSQ fit of the raw C versus $\dot{q}$ data was also tried with about the same result (refer to Figure 9). There is about a $\pm$5% spread in the curves near $\dot{q}$ = 0 with the spread becoming less than $\pm$2% at $\dot{q}$ = 20 μ l/sec. Thus, the total spread in the curves approaches the uncertainty in the data. With this in mind, the data for all pressures were fitted to a single curve giving:

$$\overline{C} = 12.77 + 0.2117\ \dot{q}$$

Note that the concentration C varies by less than 30% as $\dot{q}$ changes by a factor of about 40 to 1. Note also that the concentration cannot remain relatively constant indefinitely as the fluid delivery rate is decreased. As shown in the previous section, the atomization efficiency approaches 100% at some small but finite

value of q and thereafter is constant (i.e., 100%). As $\dot{q}$ decreases below this point, the concentration must also decrease toward zero in a linear fashion ($C \simeq constant*\dot{q}$ for fixed $\dot{Q}$) unless some other mechanism is involved.

9. Aerosol Concentration - N (Item 9, Figure 4)

    The useful atomized fluid is carried away from the atomizer as liquid droplets, a portion of which, if volatile, will evaporate into the carrier air. For this application, the solvent (water) was completely evaporated (using a diffusion drier) leaving the non-volatile component (NaCl). The dried aerosol was then passed through a neutralizer (TSI Model 3012) to minimize subsequent aerosol losses due to the inherent high charge to mass ratio that the atomization process produces when using polar solvents. The subsequent aerosol size and concentration distributions were measured (after appropriate dilution) using the TSI Electrical Aerosol Size Analyzer (EAA). The EAA had an electrical response time of a few seconds providing an indication of the snort term generation fluctuations as recorded on a strip chart recorder (c.f. Figure 5). The data acquisition system sampled the EAA output periodically and provided stability statistics for various time frames in addition to the size distribution data as represented in Figure 10.

    The concentration number N as given in Table 2 is the total count of all particles per unit volume of sampled air with diameters between approximately 0.0237 μm and 0.9 μm . The values in the table have been corrected for the dilution factor, and hence

21
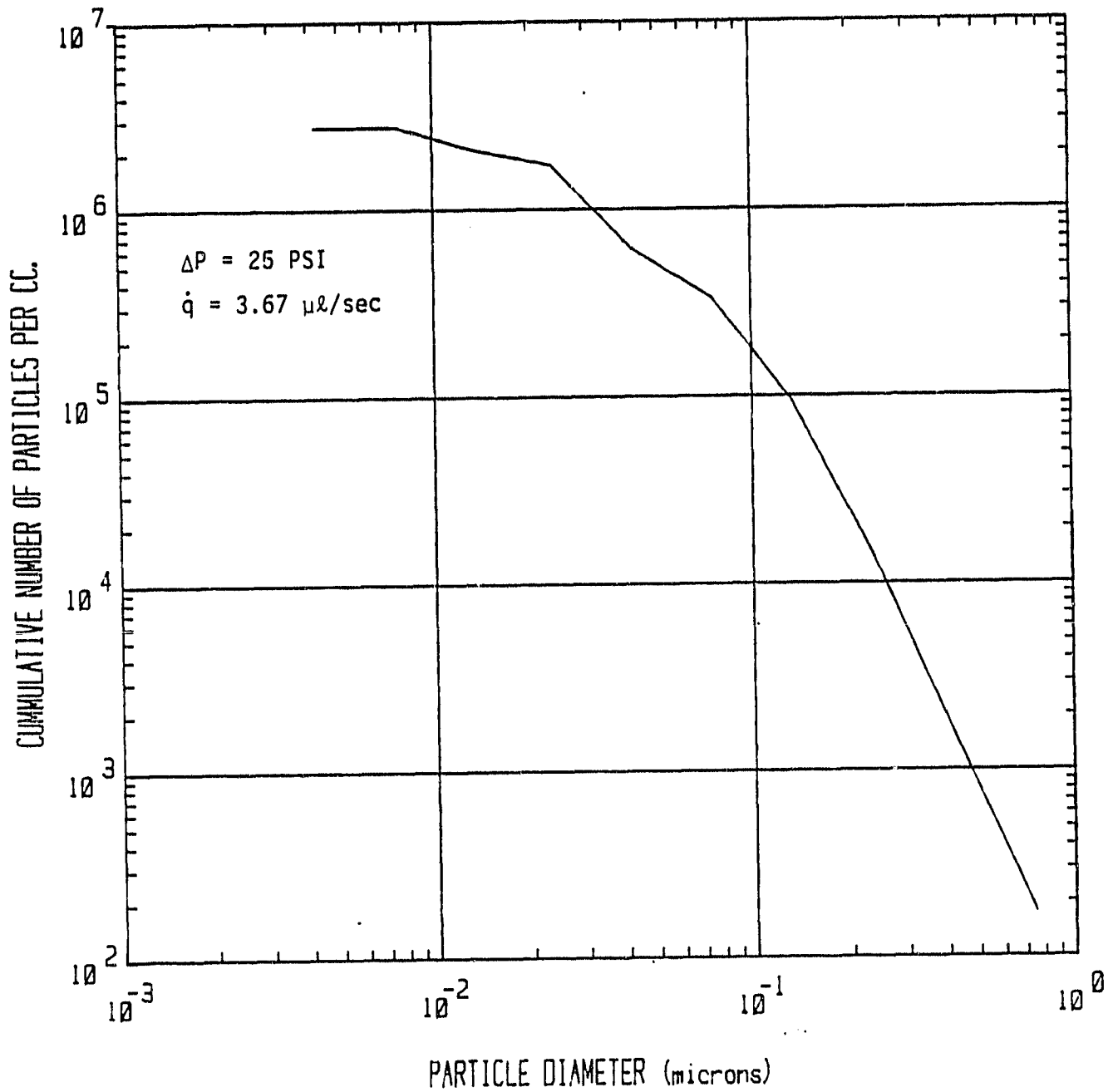
Figure 10. Aerosol Size Distribution

22

approximately represent the aerosol concentration emerging from the generator (diffusional losses although not negligible, are not taken into account since emphasis was on relative changes in parameters rather than absolute values).

The N versus $\dot{q}$ data from Table 2 are plotted in Figure 11. These curves are roughly exponential in form. Better fits were obtained from the following observations. By definition, Nd_m^3 = $\Sigma n_i d_i^3$ = mass of fluid/unit volume of air which is just proportional to the concentration C. The concentration C has been previously shown to be an approximately linear function of q, i.e., $C = a + b\dot{q}$. The next section shows that d_m^3 also varies, to the first order, in a linear fashion as $c + d\dot{q}$. Thus, the dependency of N on q can be expressed as:

$$N = kC/d_m^3$$
$$= k\ (a + b\dot{q})/(c + d\dot{q})$$

which can be reduced to the simpler form (redefining the coefficient as:

$$N = (a + b\dot{q})/(c + \dot{q})$$
$$= \text{Concentration affects/radii affects.}$$

Thus, the N variation with q is complicated by the change in the shape of the aerosol distribution (i.e., d_m) as well as the changes in the concentration itself. Figure 11 contains the resulting expressions of this latter form for each curve. The curve fit is much better than that provided by the exponetial fit. It should be noted that the assumed linear relationship (here as well as with other relationships) may only be an approximation for this

23

$$N = \frac{(4.178 - 1.234d)+(3.374+5.48d)\ \dot{q}}{(9.247 + 0.03d) + \dot{q}}$$

Orifice Size   D=13.5mil

$$d \equiv \left[1 + \frac{2}{(P_a^2+\Delta P)} \left(\frac{3.33-(P_a+\Delta P)}{(P_a+\Delta P)-2}\right)\right]^{-1}$$

35 PSI

$$N = \frac{2.96 + 8.85\dot{q}}{9.29 + \dot{q}}$$

25 PSI

$$N = \frac{3.47 + 6.50\ \dot{q}}{9.26 + \dot{q}}$$

15 PSI

$$N = \frac{4.16 + 3.37\dot{q}}{9.224 + \dot{q}}$$

ΔP

(NUMBER/CC)

$N / 10^6$

$\dot{q}$ (µl/sec)
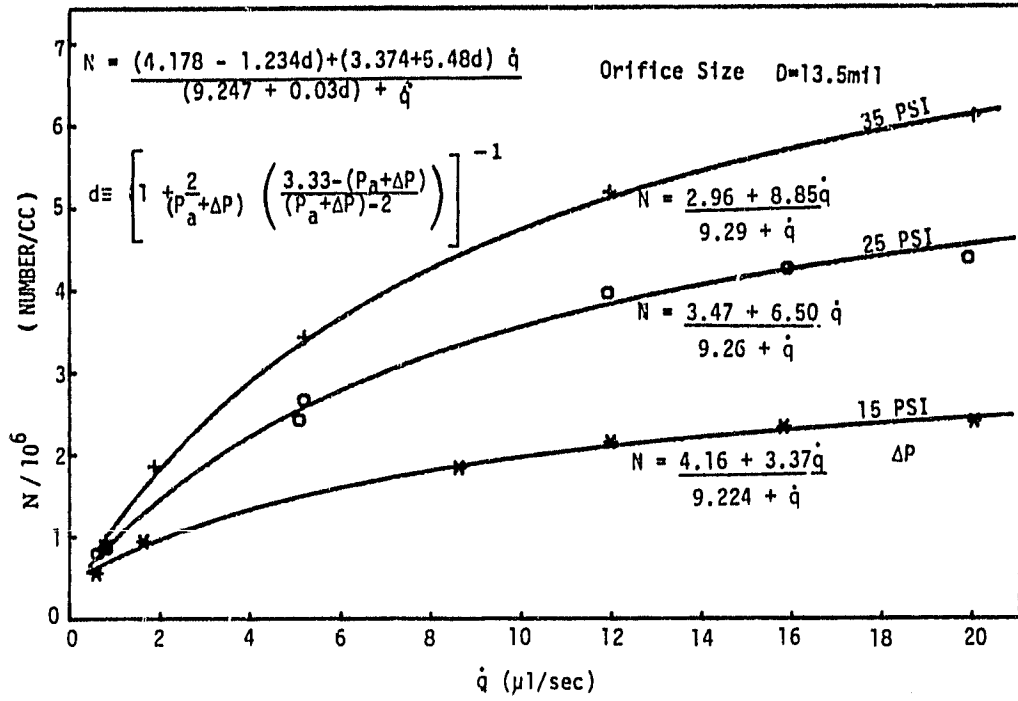
Figure 11.   Aerosol Particle Concentration

restricted data range. In most cases, the data falls within $\pm 5\%$ of the curves, hence these relationships are satisfactory for the present purpose of performance prediction over this restricted operation range.

The relationship which gave the best account for the pressure dependency evolved from the observation that the change in N due to a pressure change varied approximately as $\Delta(P_a + \Delta P)$. For a fixed $(P_a + \Delta P)$, the change in ΔN becomes smaller as $(P_a + \Delta P)$ increases. This observation gave an adjustment factor, f, of:

$$f = \left[1 + \frac{2}{(P_a + \Delta P)} \frac{3.33 - (P_a + \Delta P)}{(P_a + \Delta P) - 2} \right]^{-1}$$

where 2 and 3.33 were the lower and upper total pressure points respectively for this data set. Each of the coefficients in the (N, $\dot{q}$) relationship were fitted to a linear function of f giving the complete flow and pressure dependency of N as:

$$N = \frac{(4.178 - 1.234\ f) + (3.374 + 5.48f)\dot{q}}{(9.247 + 0.03f) + \dot{q}} .$$

25

10. Average Mass Droplet Diameter - d_m (Item 10, Figure 4)

The aerosol size distribution from this type of generator (e.g., Figure 10) can be approximately characterized by a log-normal distribution as indicated by the straight line form given in the probability plot of Figure 12. Such a distribution can be characterized by two parameters; the geometric mean (count median) diameter, d_g, and the geometric standard deviation σg. The valuesof these parameters are given in Table 2 for each data set. The relationship between these two parameters and other parameters of interest are summarized by Dennis (1976). In particular, the diameter of average mass, d_m, is given by $d_m = \ln d_g + 1.5 \ln^2 \sigma_g$. The cube of this latter parameter times the total particle number is proportional to the total mass of the fluid atomized. The magnitude of d_g in Table 2, hence also d_m, varies with $\dot{q}$ but, as with the mass concentration C, there is no apparent simple pressure dependency. A linear relationship between d_m^3 and C for each pressure is given in Figure 13 and for d_m^3 and $\dot{q}$ in Figure 14. An average d_m^3 for all data points gives: $d_m^3/10^{-3} = -0.596 + 0.1144$ C. For the restricted data range the relationship between d_m^3 and q is also approximately linear with a LSQ fit of the data giving: $d_m^3/10^{-3} = 0.845 + 0.02775 \dot{q}$ where $0.6 < \dot{q} < 20$ µl/sec (c.f., Figure 14).
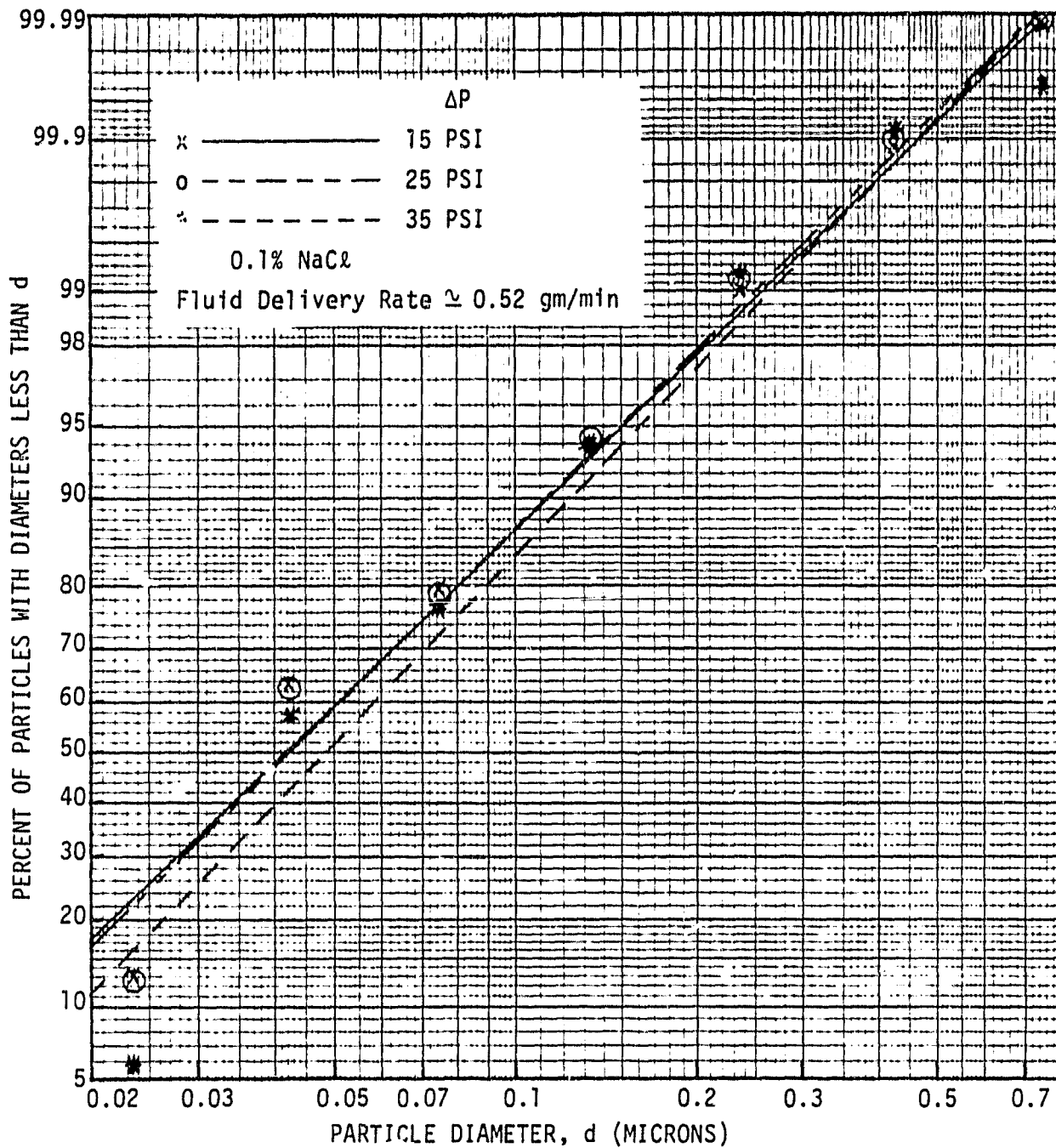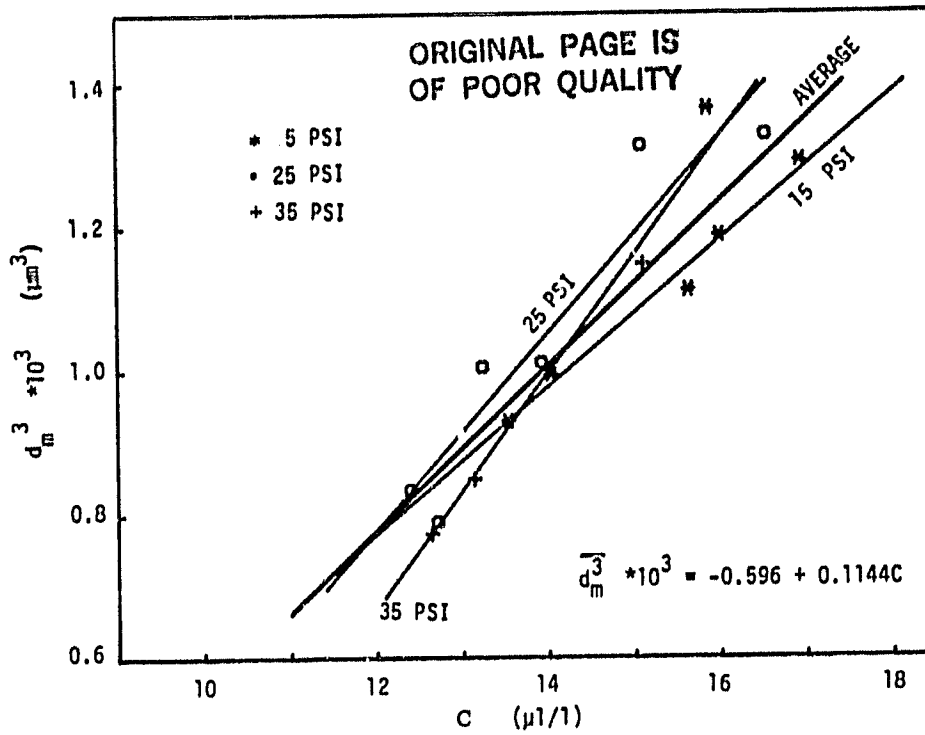
Figure 12.   Log-Normal Plot of Aerosol Distribution

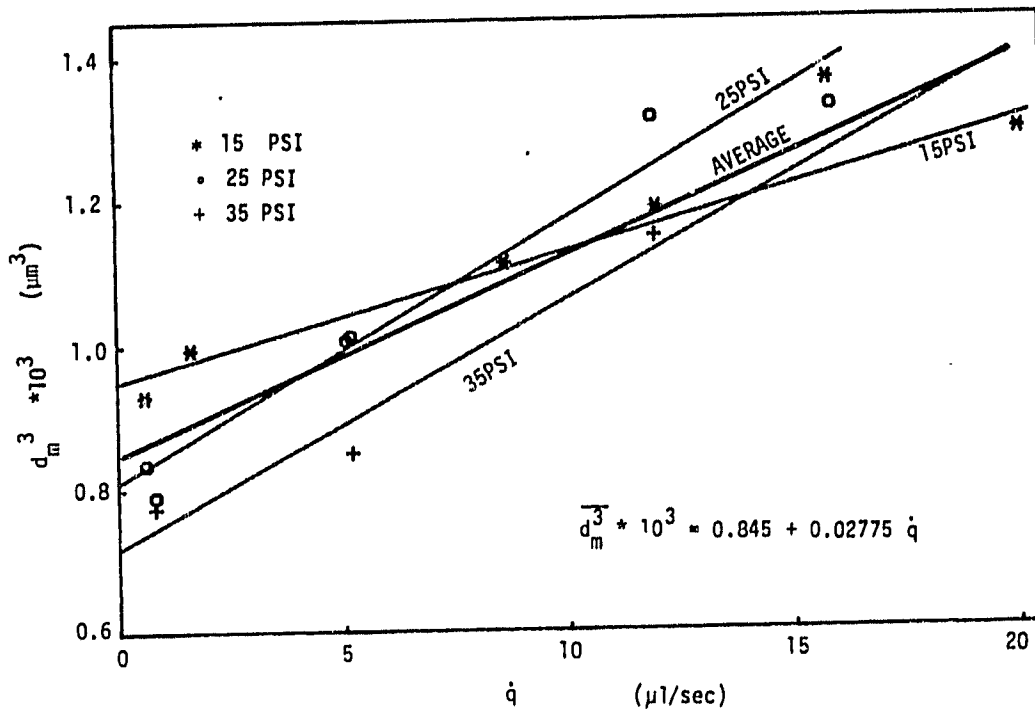Figure 13. Average Particle Volume as a Function of
Aerosol Concentration

Figure 14. Average Particle Volume as a Function of
Fluid Delivery Rate

28

11. Geometric Standard Deviation - σ_g (Item 11, Figure 4)

The geometric standard deviation, σ_g, is a measure of the width or spread of the aerosol distribution and is defined as:

$$\sigma_g = 84.13\% \text{ size}/50\% \text{ size} = 50\% \text{ size}/15.8\% \text{ size}.$$

A value of 1.0 would characterize a single size, perfectly monodispersed aerosol. The σ_g for the data sets are given in Table 2 and plotted in Figure 15. The general trend is for a slightly narrower distribution for higher fluid delivery rates and possibly for higher pressures. Although these curves appear to level out toward higher $\dot{q}$, they cannot be used to extrapolate to the unrestricted aspirated flow condition where $\dot{q}$ may be more than a decade above the flows tested with this generator. The nominal value of 2.1 for this generator is a little higher than the 1.8 as specified by TSI for their standard COA generator at $\dot{q} \approx 8$ μl/sec.

The above subsections have defined some quantitative relationships between the controlled input parameters and the resulting output parameters. Values for tne parameters $\dot{q}$ and ΔP can be selected to give the desired output, e.g., N. Section V discusses other parameters which can affect the absolute magnitude of the output parameters (e.g., orifice diameter).

The above desired relationships will now be used to ascertain the sensitivity of each output parameter on each input variable. These results should then provide guidance as to what the expected control precision requirements will be as derived from the requirements of a specific application. Although the results may not be quantitatively applicable to an atomizer of different geometric design, they should nevertheless provide qualitative guidance to the selection and procedure for quantifying the different design.
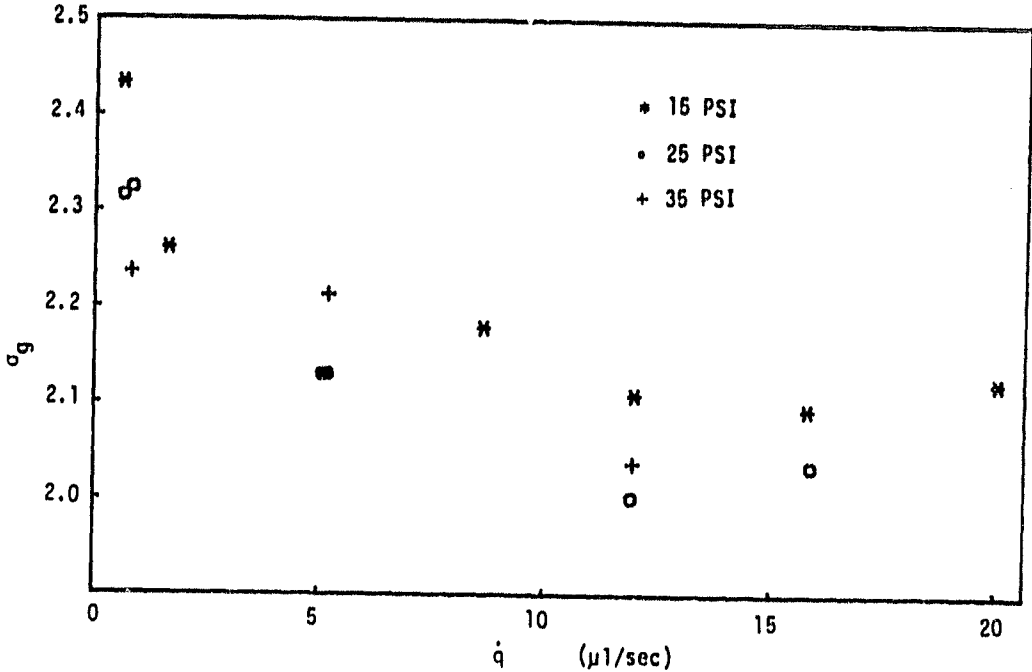
29

Figure 15.   Geometric Standard Deviation

IV. PERFORMANCE PREDICTION (PARAMETRIC ERROR ANALYSIS)

This section will determine the relative variance on an output parameter, e.g., N, as a result of a controlled (or uncontrolled) variation of the input parameters, $\dot{q}$ and ΔP. The results should permit an estimation of the repeatability, controllability and stability specifications which must be applied to the liquid and air delivery systems to assure the desired output performance.

Sensitivity Analyses

Air Mass Flow Rate ($\dot{Q}$): The air mass flow as given in Section III.5 is a function of geometric (a, c) ambient (P_a, T_0) and controlled (ΔP) quantities. Differentiating the logarithmetic gives the relative fractional sensitivities to the variables:

$$\frac{d\dot{Q}}{\dot{Q}} = \frac{dc}{c} + \frac{da}{a} - 1/2 \frac{dT_0}{T_0} + \frac{d(P_a + \Delta P)}{(P_a + \Delta P)}$$

which can be further reduced by using $a = \pi D^2/4$ to:

$$\frac{d\dot{Q}}{\dot{Q}} = \frac{dc}{c} + \frac{2d(D)}{D} - \frac{1}{2} \frac{dT_0}{T_0} + \frac{1}{(1+\Delta P/P_a)} \frac{dP_a}{P_a} + \frac{1}{(1+P_a/\Delta P)} \frac{d(\Delta P)}{\Delta P}$$

The most sensitive factor here is the orifice geometry. A one percent change in $\dot{Q}$ will occur if the effective diameter of the orifice changes by one-half of a percent or by 1.7 microns for the 0.0343 cm (13.5 mil) orifice as used for this data. Any orifice geometry change may also be reflected in the contraction coefficient c. Any blockage (by condensed moisture or debris)

31

or erosion can also cause stability problems. Such changes were observed during the preliminary generator development and resulted in the implementation of air filtration and drying procedures and the replacement of the erodible metallic orifice with a very stable sapphire orifice.

Temperature affects are somewhat diminished by the factor 0.5 and the fact that T_0 is the absolute temperature, a number in the neighborhood of 300K. A $6^{\circ}C$ increment in the temperature would result in approximately a one percent change in $\dot{Q}$. Most environmentally controlled buildings are well within that increment, hence, temperature is not a significant concern as long as the air pressure source does not appreciably modify the air temperature. Operation in an uncontrolled environment (e.g., field operations) might require special thermal control considerations. Note that $\dot{Q}$ as used in most of the analysis was in terms of volume rather than mass where one atmosphere, dry air and $T_0 = 296^{\circ}K$ were assumed in the conversion. Appropriate adjustment of the coefficient 0.0177 would have to be made if the ambient conditions are significantly different.

The fractional change in $\dot{Q}$ is equal to the fractional change in the total absolute pressure $(P_a + \Delta P)$ applied to the orifice. The multiplier associated with the ambient pressure portion of this factor varies from 0.5 to 0.3 for the range investigated, decreasing as the orifice pressure drop increases. A one percent allowable change in $\dot{Q}$ could tolerate a 3.33% to 2% change in P_a. Likewise the tolerable change in ΔP would be between 1.4% to 2%, increasing as ΔP increases. Thus, the ambient pressure must remain within 0.02 atmospheres (0.3 PSI) and the ΔP controlled to better than 0.014 atmospheres (0.21 PSI) to restrict the output flow change to less than one percent for each. An absolute pressure controller could be used, rather than the normal gauge pressure regulator, to control the total pressure, $(P_a + \Delta P)$, thus becoming more independent of ambient pressure (e.g., operation in laboratories at different altitudes).

<u>Useful Atomized Aerosol ($\dot{q}''$)</u>: Most of the relationships which have been derived are not simple product proportionalities as was $\dot{Q}$ above where the exponent of a given variable gives the relative fractional dependency between the dependent and independent variables. In order to visualize the sensitivity of the dependent variable $\dot{q}''$ on the parameters $\dot{q}$ and $(P_a + \Delta P)$, a graphical approach was selected. In most applications, the quantity of interest is the percent error in the output parameter. Thus, the fractional change of the dependent (output) variable was computed relative to fractional changes in the independent variables. The procedure is as follows. The change $d\dot{q}''$ in a parameter $\dot{q}''$ ($\dot{q}$, $(P_a + \Delta P)$ is given by:

$$d\dot{q}'' = \frac{\partial \dot{q}''}{\partial \dot{q}} \, d\dot{q} + \frac{\partial \dot{q}''}{\partial (P_a + \Delta P)} \, d(P_a + \Delta P)$$

$$= A \, d\dot{q} + B \, d(P_a + \Delta P)$$

33

The fractional sensitivity of $\dot{q}''$ relative to a fixed absolute error in $\dot{q}$ (assuming $d(P_a + \Delta P) = 0$) is given by:

$$(d\dot{q}''/\dot{q}'')/d\dot{q} = A/\dot{q}''$$

and similarly the variable sensitivity to a fractional change in the independent variable (percent change of the dependent variable for a percent change in the independent variable) is given by:

$$(d\dot{q}''/\dot{q}'')/(d\dot{q}/\dot{q}) = A\,\dot{q}/\dot{q}''.$$

This procedure was also used for the independent variable $(P_a + \Delta P)$ with $d\dot{q}$ = 0. In the actual application, both of these parameters change independently and the total random error will be a root means square of the two errors, i.e.,

$$\sigma_{\dot{q}''} = A^2\sigma_{\dot{q}}^2 + B^2\,\sigma_{(P_a+\Delta P)}^2$$

Note that the square of the coefficients A and B determine the relative weights, hence the contribution of the respective parameters $\sigma_{\dot{q}}$ and $\sigma_{(P_a+\Delta P)}$. Plots of the relative sensitivities, e.g., $(d\dot{q}''/\dot{q}'')/d\dot{q}$ vs. $\dot{q}$ were prepared which gave an indication of the relative importance of the absolute values of $\dot{q}$ and $(P_a + \Delta P)$. A more useful approach is to determine the percent change in an independent parameter that would produce a one percent change in the dependent quantity to be evaluated, e.g., setting 100 $d\dot{q}''/\dot{q}''$ = 1%. Thus, the relationships used were as follows:

The allowable percent of reading (POR), is given by (assuming 100 $d\dot{q}''/\dot{q}''$ = 1%):

$$(d\dot{q}/\dot{q})\ (\%) = (d\dot{q}''/\dot{q}'')\ (\%)/(A\dot{q}/\dot{q}'')$$

$$= 1/(A\dot{q}/\dot{q}'').$$

The percent of full scale (PFS) can also be evaluated from:

$$(dq/20)(\%) = 1/(20A/\dot{q}'')$$

where the full scale value of 20 µl/sec is used for $\dot{q}$.

Similarly, the pressure relationships give $((P_a + \Delta P)_{FS} = 3.33)$

POR: $(d(P_a + \Delta P)/(P_a + \Delta P)) = 1/(B(P_a + P)/\dot{q}'')$ and

PFS: $(d(P_a + \Delta P)/3.33)\ (\%) = 1/(3.33\ B/\dot{q}'')$.

These latter relationships are plotted in Figure 16. The ordinate is the percent error that the parameter $\dot{q}$ (or $(P_a + \Delta P)$ would need to produce a one percent error in $\dot{q}''$.

From Figure 16, the permitted (PFS) error in controlling q is between 3% and 6% being only slightly dependent on the flow $\dot{q}$. On the other hand, lower q greatly increases the permitted POR error.

From the pressure curves, higher pressure $(P_a + \Delta P)$ is a little better for the PFS case but lower pressure is better for the POR case. Lower $\dot{q}$ also results in a larger tolerance of pressure changes.

For the usefully atomized fluid $\dot{q}''$, the general indications are that the stability is favored by lower $\dot{q}$ and lower $(P_a + \Delta P)$ values. For a one percent stsbility in $\dot{q}''$, the $\dot{q}$ should be controlled to better than 3% of FS (worse case) and the pressure to approximately 0.7% of FS (worse case). Corresponding specifications for values other than one percent output change can be obtained by directly scaling the appropriate values.

Atomization Efficiency (E): The sensitivity analysis approach as discussed for $\dot{q}''$ was also performed for the atomization efficiency E. The permissable errors in the parameters $\dot{q}$ and $(P_a + \Delta P)$ are given in Figure 17 where an error of one percent of reading was assumed for each parameter. In general, larger errors are permitted for larger $\dot{q}$ values. The allowable PFS q error
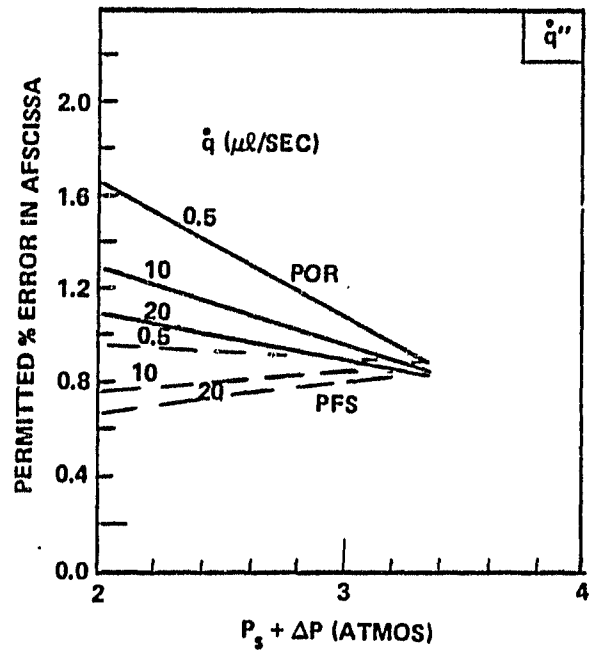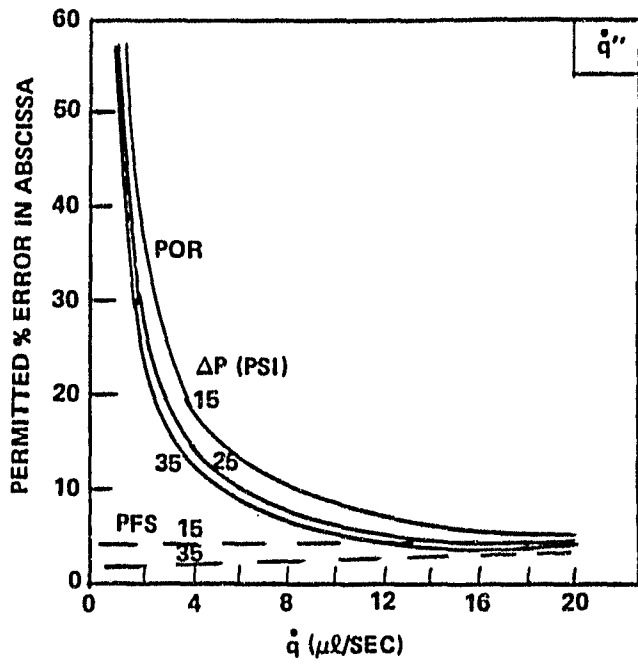
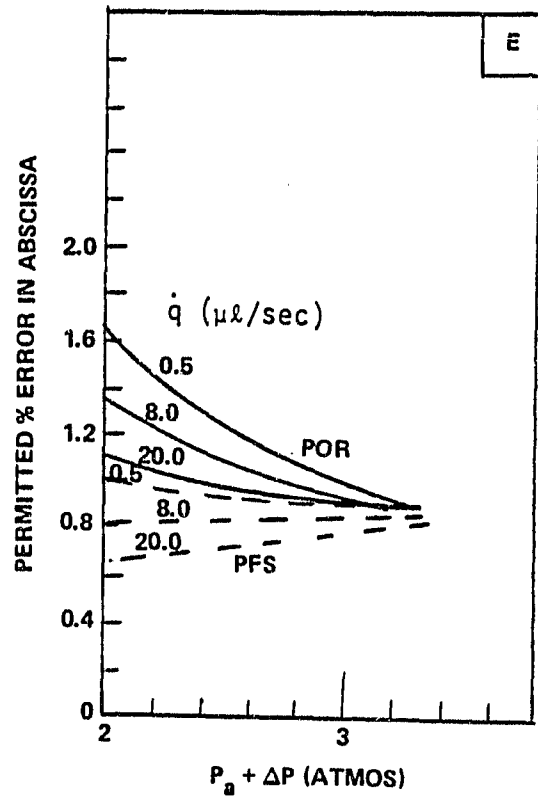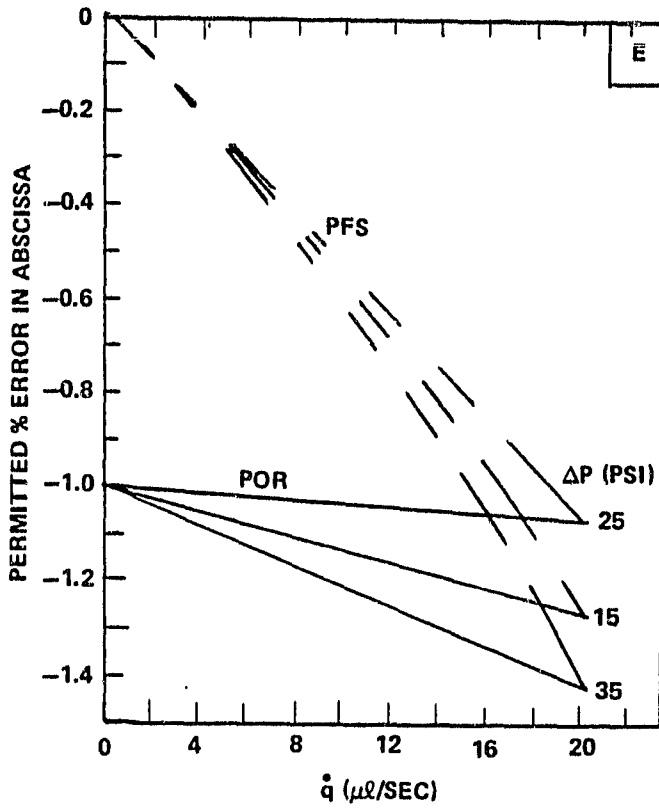Figure 16. Permitted Control Error for 1% Change in Useful Atomized Aerosol

Figure 17. Permitted Control Error for 1% Change in Atomization Efficiency

could be very demanding on the flow controller, down to 0.025% for $q = 0.5$ μl/sec. Control on the fluid delivery rate approaching 1% of setting must be maintained to assure less than 1% instability in the atomization efficiency.

The PFS pressure control requirement is not quite as severe, being around 0.7% to 1.0% with lower flows permitting even greater leeway. The POR tolerances are somewhat relaxed as the operating pressure or fluid flow rate decreases. In the regime where $E = 100\%$, the efficiency stability becomes insensitive to pressure changes, but varies on a one to one basis with fluid flow changes.

Aerosol Volume Concentration (C): The sensitivity analysis results for C are summarized in Figure 18. As noted in previous discussions, the concentration is relatively insensitive to changes in the fluid flow and pressure. The fluid flow would only have to be held to better than 2.4% of full scale to limit the concentration changes to below one percent. As noted in Figure 18, a much larger latitude is permitted for the POR specification.

At the lowest pressure settings, the pressure control would need to be on the order of 1.5% of FS. Larger pressures permit relaxed pressure control stability for this particular output parameter. This is primarily due to the compensating changes in efficiency and total air flow which occur whenever the pressure changes. For the present set of data, there is a region (2.9 to 3.2 atmospheres) where the effects of a change in the total pressure are greatly attenuated and thus are not reflected in the output concentration. The absolute magnitude of the attenuation factor should not be
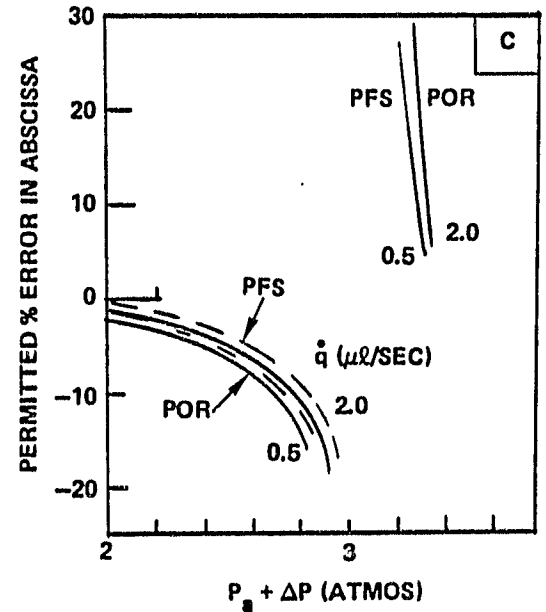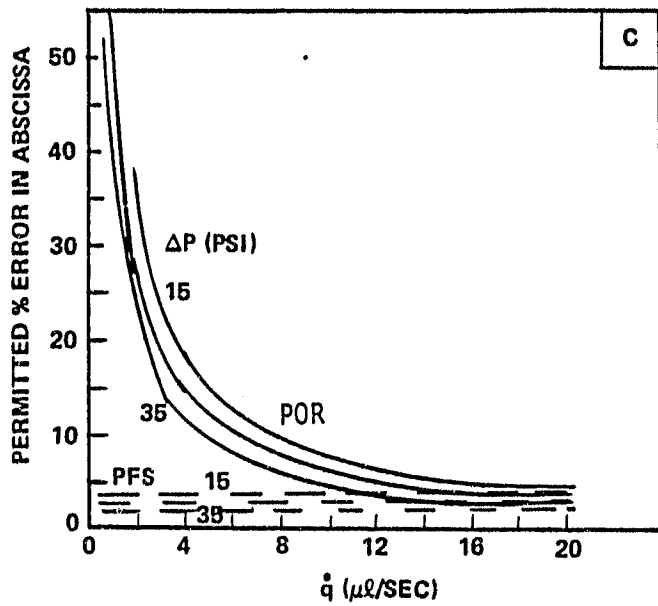
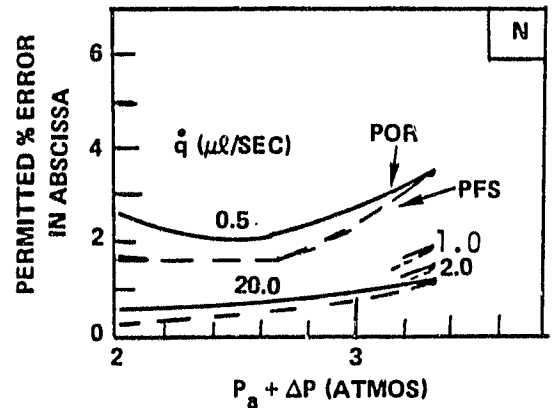Figure 18. Permitted Control Error for 1% Change in Aerosol Volume Concentration

Figure 19. Permitted Control Error for 1% Change in Aerosol Number Concentration

taken seriously as it is highly dependent on small differences in the data. A more extensive data base would be required to further verify if this regime is real and to quantify its extent. In the region of $E = 100\%$, C will be directly related to changes in the fluid flow and the total pressure, thus requiring closer control of both.

Aerosol Number Concentration (N): Figure 19 summarizes the N sensitivity analysis. Changes at larger flows have less effect (large tolerable changes) on the number concentration output with slightly better conditions at concurrent lower pressure. The PFS stability requirements for q at low $\dot{q}$ is very demanding indicating potential problems in providing high stability near the 100% region. Flow control devices which specify percent of full scale must be selected with the full scale point as close to the operating point as possible. For example, full scale range of 10 µl/sec rather than 20 µl/sec would permit around a 2% variance rather than less the 1% at 8 µl/sec. Pressure change effects are minimized at lower q values. Pressure control to a half percent of full scale at high fluid delivery rates to 1.5% or more of full scale at low delivery rates are required to limit the N variation to less than one percent. In the 100% efficiency regime, both the fluid and the pressure controls requirements will probably be tighter.

Diameter of Average Mass (dm): The diameter of average mass is relatively insensitive to changes in fluid flow $\dot{q}$. Figure 20 summarizes the sensitivity analysis for d_m. A four percent of full scale control on q would be sufficient to limit the dm changes to values under one percent. Comparable stability on d_m^3 would require a factor of three tighter control

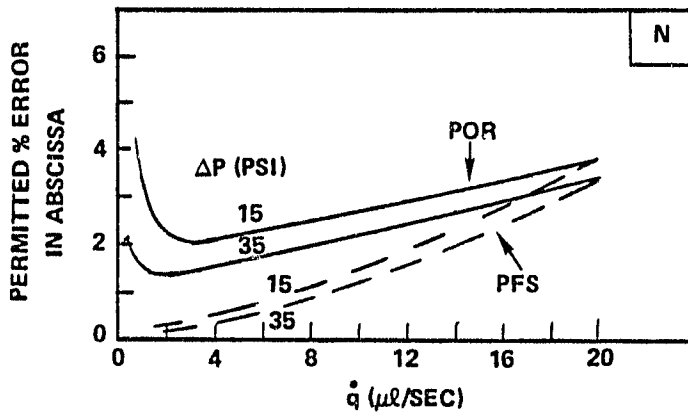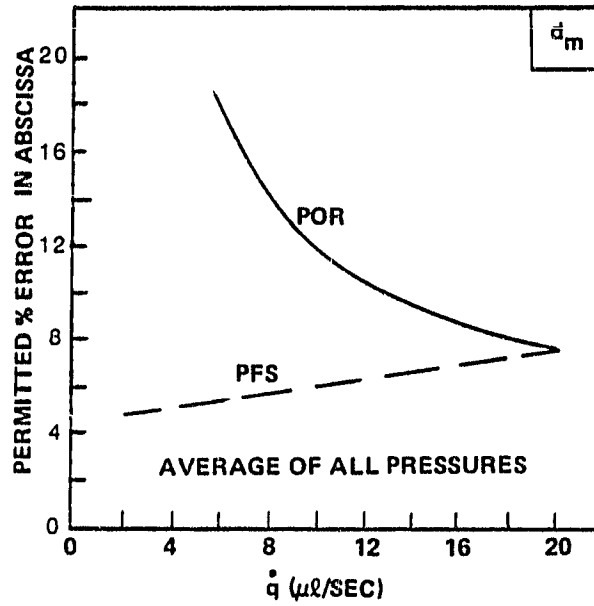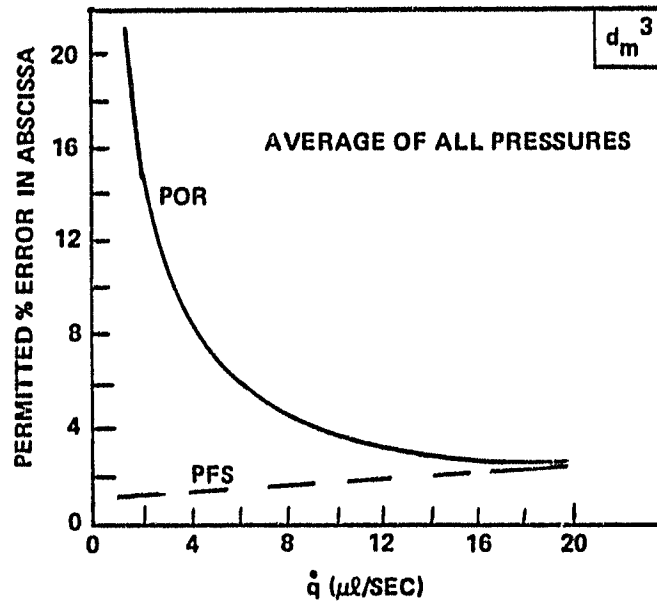Figure 20. Permitted Control Error for 1%
            Change in Aerosol Average Mass

40

specification for $\dot{q}$. The pressure dependency is not as apparent but data indicates that a couple of percent at high flows and three or four percent at low flows would be acceptable for d_m control to 1%. The pressure versus d_m exhibits cross over regimes as did C versus $\dot{q}$, hence, there may be a point where the pressure affects are minimized.

Summary of $\dot{q}$ and $(p_a + \Delta p)$ control requirements: Atomization efficiency and air flow rate produce compensating affects which minimize output concentration changes when the atomizer pressure changes.

The total useful mass output, $\dot{q}''$, is fairly sensitive to total pressure changes at both low and high fluid flow rates (a little better at low flows) as also is the total particle concentration N. Ambient pressure changes are reflected in a change in the pressure across the orifice, hence if the ambient pressure is expected to change significantly, the pressure across the orifice may have to be controlled even more closely.

The mass concentration C and diameter of average mass $\bar{d}_m$ are both relatively insensitive to pressure changes, mid pressure being somewhat better. Lower $\dot{q}$ also provides best control.

See Table 4 for a summary of the control requirements.

TABLE 4. Parameter Control Requirements Summary

Summary of control requirements in $\dot{q}$ and $(p_a + \Delta p)$ to assure ≤ 1% change in the output parameters specified. The values in the table are percent of setting (reading). Left value in low independent variable range and right number is for high range.

	$\dot{Q}$	$\dot{q}''$		E		C		N			$\bar{d}_m$	
$\dot{q}$	-	> 50	3-4	1	1.08	> 50	3-4	2-4	1.5	3	> 50	> 2
$(p_a + \Delta p)$	1	1.1	0.8	1.1	0.8	2-3	>>50 10	< 1		1	3	2
T_o	2	*NE		NE		NE		NE			NE	
D	0.5	NE		NE		NE		NE			NE	

* NE NOT EVALUATED

V. OTHER FACTORS

During the development of an aerosol generator which would perform reliably in a low-acceleration environment, several improvements to the physical design were made. These factors were not quantified in detail as those in the foregoing discussions. A configuration was selected that gave acceptably stable results with minimal attempt to optimize the factor's contribution to the overall performance. Nevertheless, these factors are significant relative to the overall performance and stability of the Collison type of generator and will be summarized.

Orifice rotation (eccentricity) - During the course of removing and replacing of the orifice plate in the aerosol generator, differences in the generated number concentration output were observed (this being the primary quantity of interest for the cloud physics related application). As mentioned previously, sapphire orifices were used to eliminate initial orifice irregularities and eventual erosion. The orifice assembly consisted of a sapphire orifice mounted in a relatively thick, 0.953 cm (3/8") diameter, stainless steel disc. These orifice assemblies were blown up optically by a factor of about five using an optical comparitor. Polar graph paper was centered over the orifice center and the outline of the metal assembly traced. This procedure showed that the orifices were not all mounted at the exact center of the metal mounting disc. One of the better 0.0254 cm (10 mil) orifices was rotated in steps with the resulting EAA output recorded. Figure 21 illustrates that the output of the unmodified orifice varied by less than ten percent as it was rotated. This orifice assembly was then machined
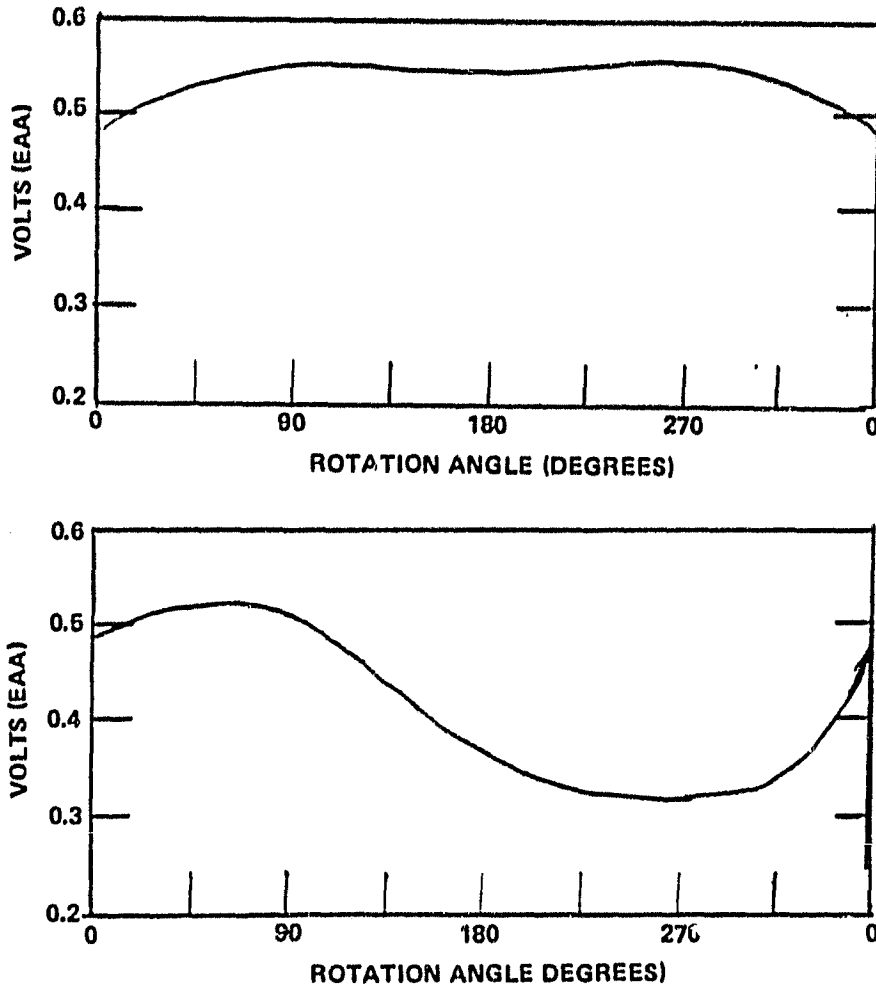
42

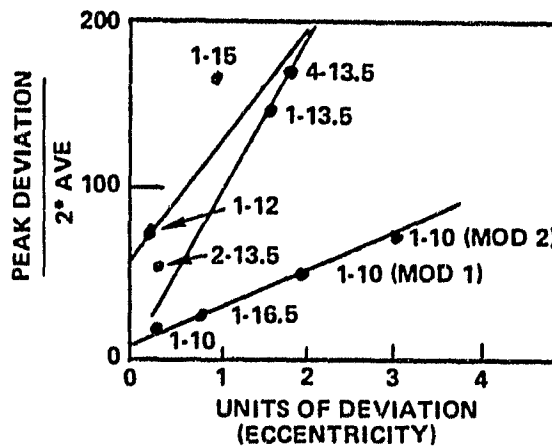Figure 21. Total Aerosol Concentration as a Function of Orifice Rotation

Figure 22.   Aerosol Concentration Change as a
Function of Orifice Eccentricity

43

on one edge to make the orifice acentric and then recharacterized, the results are as given in Figure 21. The variation was now about 40 percent as the orifice plate was rotated. Other orifices showed a five to one change. Figure 22 summarizes the data collected for various orifices showing an increase in output variation as the eccentricity (off centeredness) is increased with peak output occurring when the orifice is nearer to the fluid injection point. This increased output (increased efficiency) is felt to occur as the center of the air jet (orifice) is moved closer to the point of fluid injection, hence providing a better coupling between the air kinetic energy and the fluid to be atomized. This factor was also approached qualitatively from another direction. For a centered, concentric orifice, the fluid injection point was extended upward toward the center of the orifice air stream using small tubing. An increase in number concentration (greater than a factor of two) output was observed as the fluid injection point approached the approximate center of the air stream and decreased as it passed this point. A flush injection geometry was used to avoid unnecessary design complexity. Another important factor identified was that of keeping the fluid injection opening as small as feasible to avoid random extraction and refilling by the turbulent air stream. This is particularly important at low fluid flows where the atomization efficiency becomes largest.

Wick surfaces - The aerosol impaction zone and much of the area around it was covered by a wicking surface as was necessitated by the intended application in a low acceleration environment where gravity drainage would not suffice. This surface was observed to enhance the output stability but

44

decreased the total output concentration, N, by about 40% (Figure 23) as compared to all stainless steel and all plastic versions of the generator. The clear plastic unit permitted observations which indicated irradic gravity drainage of the fluid from the impaction surface and areas above the direct impaction area. This irregular drainage caused changes in the fluid film coverage in the impaction zone, hence changes in the quantity of impacting aerosol which was retained by the surface. This variation has also been observed by TSI and the Desert Research Institute (University of Nevada, Reno). Even though some output is sacrificed, this wicking surface, should also be added to the generators intended for terrestrial applications to enhance performance stability.

Pulsation affects - The fluid delivery pump used for these tests was very stable but supplied the fluid in pulses, about one per second with a supply duty cycle of around 30 percent. This delivery characteristic caused the peak fluid delivery rate to be some three times above the average delivery rate. The output stability as averaged over several seconds did not suffer from this pulsation but the aerosol number concentration, N, decreased by some 30 to 40 percent. This decrease in output can be expected by looking at the N curves of Figure 11. The higher intermittent flow would give a higher instantaneous output, but the averaged output would be roughly one-third of this peak value (30% duty cycle) giving a resultant decrease of some 40 to 50%. Hence, a smooth constant delivery enhances the N output.

Fluid Pump - A fluid delivery system must be selected that is constant from second to second and minute to minute. A small gear type pump that was assessed had significant back leakage which varied with time and was found to be unsatisfactory. Two syringe type fluid delivery systems were tried initially and both were found to have unacceptably high output variations with
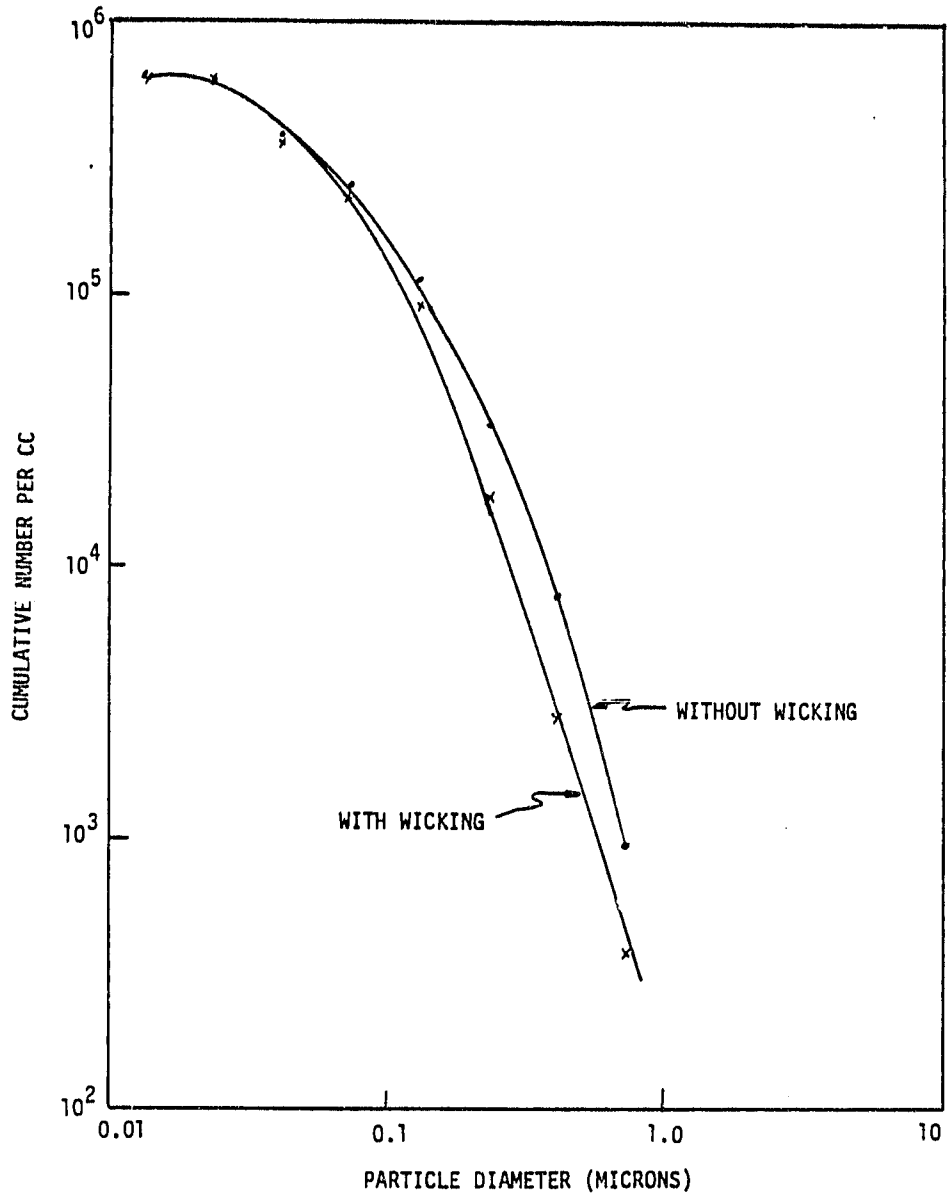
45

Figure 23. Affects of Wicking

at least one of them being due to the gear drive mechanism. These units also did not provide the unattended operating time that was required. The rotating piston-pump (Fluid Metering Inc.) proved to perform satisfactorily for hundreds of hours and was used with an in-house designed bellows pulse suppression unit (operated at about one-fifteenth of an atmosphere back pressure). Parastolic type fluid pumps may work equally well but were not tried or selected for this particular application because of the potential need for periodic tubing replacement.

Impaction distance - The distance from the exit of the constrained air flow to the impaction point affects the output of the generator as summarized in Figure 24. The characteristic droplet diameter is smallest at close impaction distances of 0.3175 cm (1/8") and becomes larger with larger separations with a somewhat leveling out for separations greater than 2.54 cm (1 inch) as would be expected from considerations of particle inertial/impaction affects. The nominal value of 1.27 cm (0.5 inch) used by TSI was chosen for this application.

Dry air - The rapid expansion of the air passing through the orifice causes cooling of the surrounding area including some of the upstream structure. Removal of the orifice plate at times of very high generation instabilities resulted in the detection of moisture collected on the orifice plate. Removal of this moisture restored the generator to its previous stability level. This condensed moisture causes sporadic blockage of the orifice, and as has been shown in the sensitivity analysis, has very significant effects on the air flow rate and hence on the output parameters. The air must be dried and filtered to assure that moisture condensation and particulates do not interfere with the generator performance.
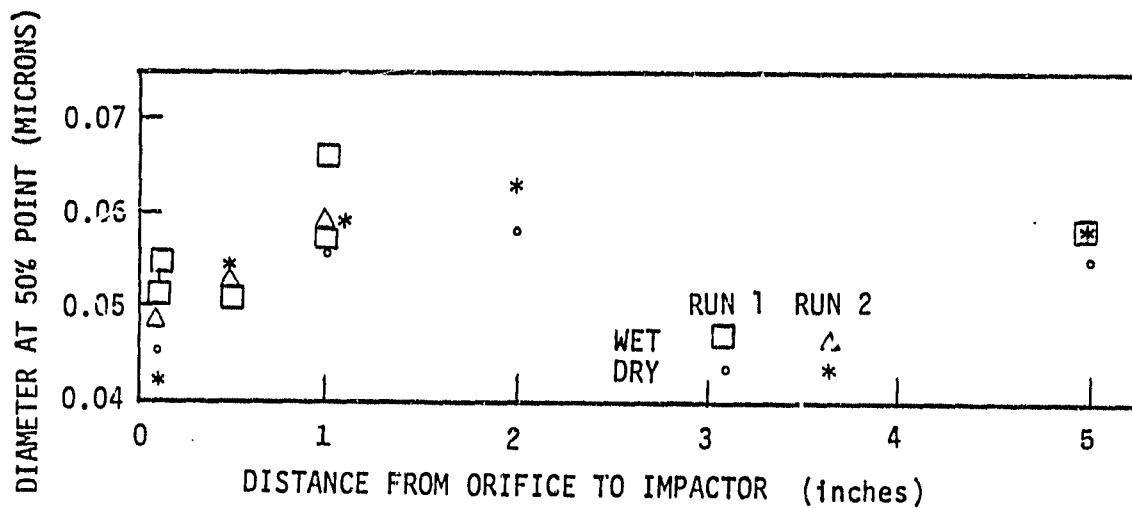
47

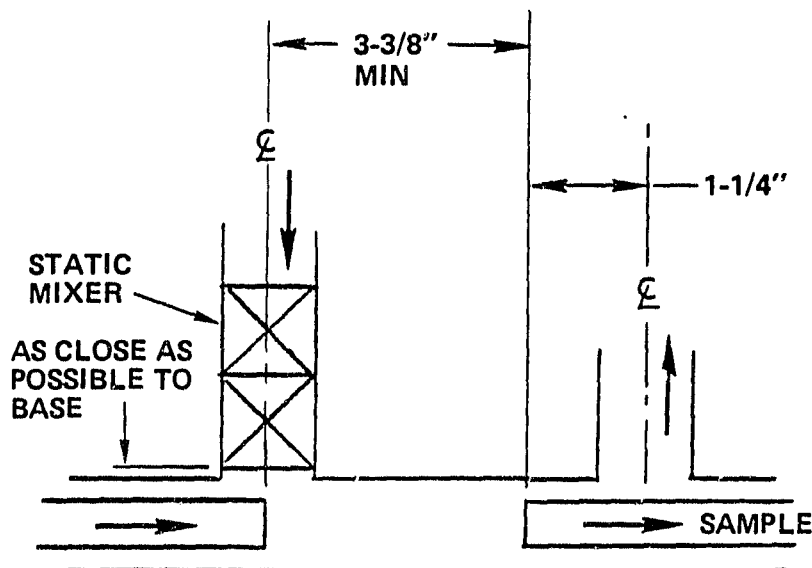Figure 24. Affects on Geometric Mean Diameter Due to Impaction Distance

Figure 25. Aerosol Diluter Configuration

Aerosol dilution - Often the aerosol concentration emerging from the generator must be reduced, or the total air flow increased, for a given application. These objectives are satisfied by combining the generated aerosol stream with a clean, dry air supply, hence resulting in a dilution of the aerosol concentration. Considerable fluctuations in the aerosol characteristics can be caused by improper dilution procedures. Figure 25 illustrates an approach which has given very good results. Key points include bringing the clean air in at right angles to the aerosol flow, using turbulators and the right angle turn to produce a turbulent inflow. The aerosol stream is injected near the center of this "T". Additional turbulators can be added downstream, an approach which is necessary if the flow rates are high and the distance to the measurement or use-point is short. If sampling of this combined flow is to be performed, special precautions must again be observed. The sampling point should be coaxial and near the center of the flow and at least several diameters upstream of any major bend in the main flow tubing. Insufficient care in this portion of the system will often give erroneous indications of generator instabilities when actually the dilution and/or sampling procedure is at fault.

Neutralizer - Any nebulization approach of high dielectric fluids (e.g., water) results in particles with very high charge to mass ratios. This ratio is further increased when the solvent is evaporated leaving an insoluble solute as the final desired particle. The recommended procedure is to diffusion dry the aerosol first and then pass it immediately through a neutralizer. This sequence gives the minimum charge to mass ratio since the

49

final residing charge is a function of particle size at time of neutralizing. If drying will occur in a large residence volume such as a chamber, then the aerosol should be neutralized prior to injection into this volume to minimize coagulation and wall losses of the aerosol.

The above factors were found to be of enough importance that they had to be resolved before the basic generator stability problem could be effectively attacked. Hence, the full system must receive careful consideration.

VI. CRITICAL PARAMETERS SUMMARY

As shown in the previous sections, pressure regulation will most often be the parameter requiring the tightest control. This air must also be dry and filtered to avoid problems at the orifice. Fluid flow control is also important and is an area that is often difficult to implement, especially in the low fluid flows that are required for these types of aerosol generators.

On the physical side of the generator design, consistent wetting of the impaction surfaces can significantly enhance output stability with some possible sacrifice in the output magnitude. Orifice wear can cause short term fluctuations and long term output changes, but the sapphire orifice provided an inexpensive and excellent solution to this problem. The handling of the aerosol after generation can introduce significant variations which are often mistakenly attributed to the generation process itself.

As has been shown, the output efficiency of this type of atomizer can be brought to near 100% with nominal loss in output concentration or useful mass of fluid atomized. On the other hand, the higher efficiency conditions may be opposed to high particle number concentration. Both fluid flow rate and pressure can be manipulated to optimize the specific output parameter for a given application.

VII. <u>REFERENCES</u>

Neste, S. L., and L. R. Eaton: <u>Phoretic Motion Experiment-
    Final Report</u>. NASA/MSFC contract number NAS 8-33149.
    September 1981.

Hudson, J. G. and P. Squires: Evaluation of a continuous
    cloud nucleus counter. <u>J. Applied Meteorology,</u> 12, 175-183.
    February 1973.

PART B

ZERO-G CFD CHAMBER PERFORMANCE

1.0 INTRODUCTION

During the NASA sponsored ACPL (Atmospheric Cloud Physics Laboratory) program, a computer simulation program was developed for the CFD (continuous flow diffusion) chamber. A characterization of a CFD chamber in zero-gravity was not completed due to program cancellation. This chamber simulation program was more extensive than any previous programs of this type. The computer program is not only able to provide useful zero-g information but can also simulate the one-g horizontal mode.

The following sections have been written to record some of the characteristics of a CFD chamber which would be useful in terrestrial as well as in future zero gravity applications. The areas briefly touched include: a) graphical estimation of the time to reach a given critical supersaturation ,S_c, given chamber wet/wet zone midpoint setting Sm; b) nomograph of the chamber supersaturation profile including the displacement from the centerline of the peak supersaturation; c) theoretical growth times · in zero-g for non-vapor depletion conditions for three temperatures, $5^{\circ}C$, $15^{\circ}C$ and $25^{\circ}C$ with specific emphasis on high accuracy data; d) depletion depending on droplet size distribution and e) some aspects of chamber operation and associated constraints for the 1-g horizontal mode.

The above areas have not been exhaustively studied, but the present results should prove both interesting and useful to those who use the CFD (and to some extent the static diffusion liquid, SDL) chamber.

2.0 SUPERSATURATION BUILDUP TIME

The initial RH at the start of the wet/wet zone must be known in order to determine the rise time of the humidity to a given critical supersaturation in the wet/wet zone.

2.1 Wet/Dry Zone Equilibrium RH

The equilibrium relative humidity from the computer simulations for the wet/dry zone of the CFD chamber were compared with theoretical values based on the temperature difference between the wet and dry chamber plates. At $5^O C$ the centerline wet/wet zone conditions of Sm = 0.1%, 0.2%, 1% and 10% were checked with 10, 30 and 50 zones between the plates and at $25^O C$ for 0.16%, 0.2%, 0.4%, 0.6%, 0.8%, 1.0%, 2.0% and 10% S_ms. These simulation runs agreed within two to three decimal places with the theoretical values as obtained using water vapor pressure data from the Smithsonian Meteorological Tables. The equilibrium wet/dry zone RH values for $5^O C$ and $25^O C$ were equal, for the same S_m, to one part in a thousand (for $0.1 < S_m < 1.0\%$). The data is plotted in Figure 2-1.

2.2 Time To Reach RH in the Wet/Wet Zone

The number of time constants required to go from an initial RH_o to a given RH where the final equilibruim RH is RH_F is approximately given by:

$$t/\tau = (\log_{10} e)^{-1} \log_{10} [(RH_F - RH)/(RH_F - RH_o)]$$

$$\text{or} \quad (RH_F - RH)/(RH_F - RH_o) = e^{-t/\tau}.$$

The modelled supersaturation versus time is plotted in Figure 2-2. Three values of RH must be specified to determine the required number of time constants. From the previous section, the initial (dry/wet zone) RH_o is
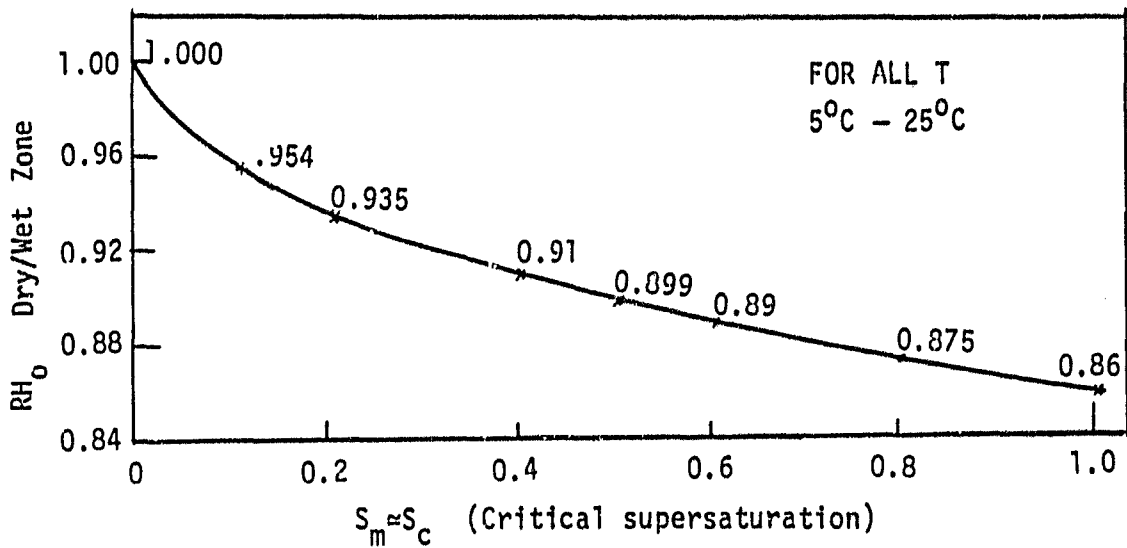
2

Figure 2-1. Dry/Wet Zone Equilibruim Centerline RH

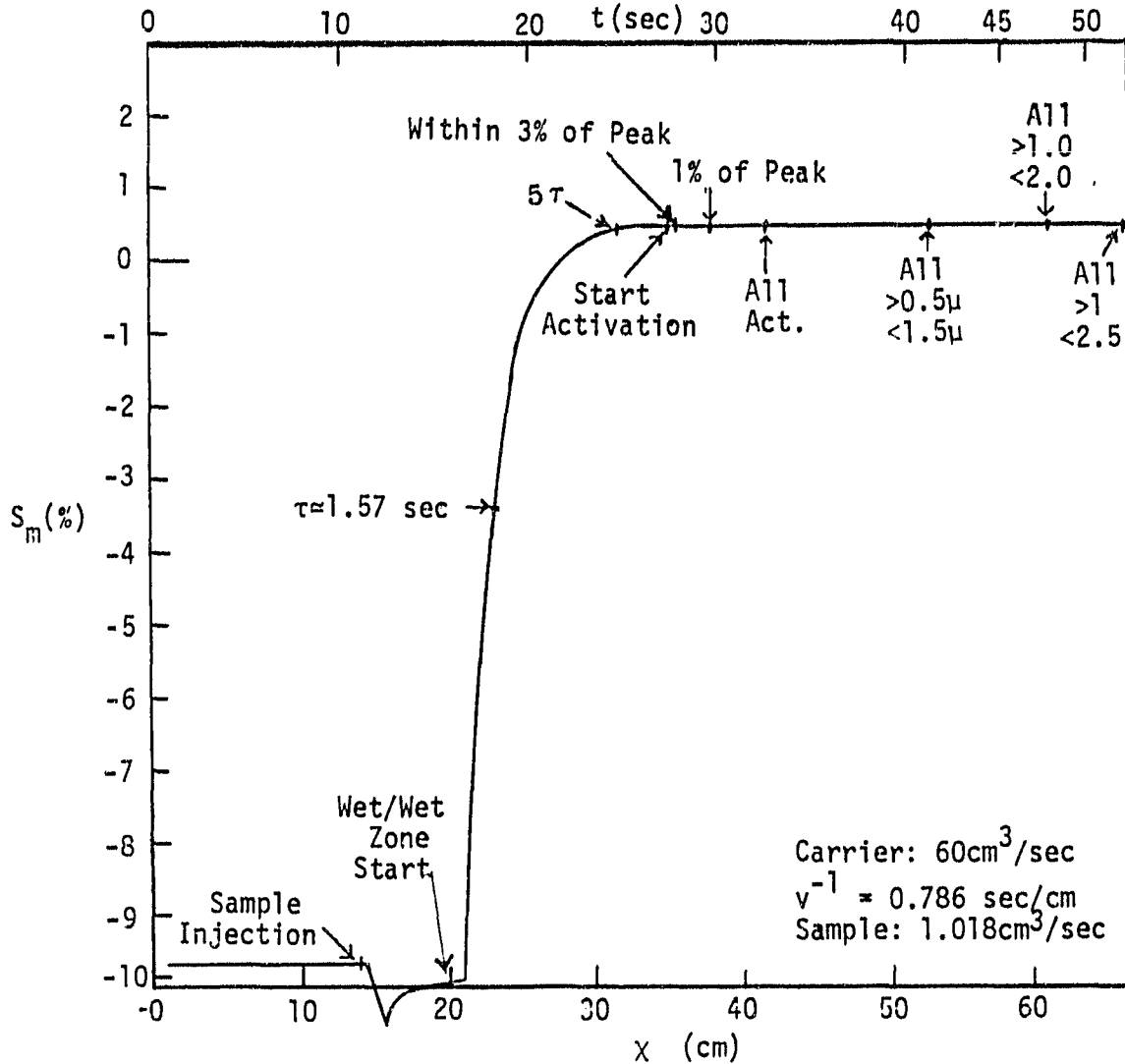Figure 2-2. RH Transition Profile Between Wet/Dry and Wet/Wet Zones

related to the final RH, RH_F (or S_m), hence the number of independent variables can be reduced from three to two. As seen from the above equation, the number of time constants is dependent on the fractional distance that the desired RH is relative to RH_F and RH_O, i.e., $(RH_F-RH)/(RH_F-RH_O)$. Technically, an infinite time is required to exactly have RH $= RH_F$ thus the time to reach within a specified nearness to RH_F is used. For the CFD chamber applications, the time to reach the nucleus's critical supersaturation S_c (which is below the chamber equilibruim S_m) is of interest. The haze particle formed on this nucleus can not grow into a droplet until the RH exceeds S_c. Assume that S_m is above S_c by some amount defined by: Excess = $E(\%)$ = $100(S_m-S_c)/S_c$, Hence:

$$t/\tau = -\ln \left[(RH_m - RH_c)/(RH_m - RH_o) \right]$$

$$= -\ln \left[(S_m - S_c)/(S_m - S_o) \right]$$

$$= -\ln \left[(1 - (1 + E/100)^{-1})/(1 - S_o/S_m) \right]$$

This relationship is plotted in Figure 2-3 as the number of time constants ,(t/τ), that are required for RH to build to S_c for given S_m.

The dashed lines in Figure 2-3 are for fixed percent excess supersaturation, e.g., 1%, 3% etc. Note that when the excess is large (i.e., 90%) the number of time constants is a minimum of three to four for 0.1% < S_m < 1% and 0.1% < S_c < 1%. As the excess decreases, the number of time constants to reach S_c increases reaching 7.5 to 8 time constants for a 1% excess. Thus as higher accuracy data are required from the chamber (i.e., as all nuclei are activated, S_c approaches S_m resulting in lower excesses) longer times are required before the nuclei can grow as droplets. A problem, that will be discussed later, arises when the larger nuclei (low S_c) begin to grow but the smaller nuclei (large S_c) are unable to grow (c.f., the sharp upturn of the curves in Figure 2-3 as S_c approaches S_m). In a polydispersed distribution the larger nuclei grow and fall out in a one-g

4
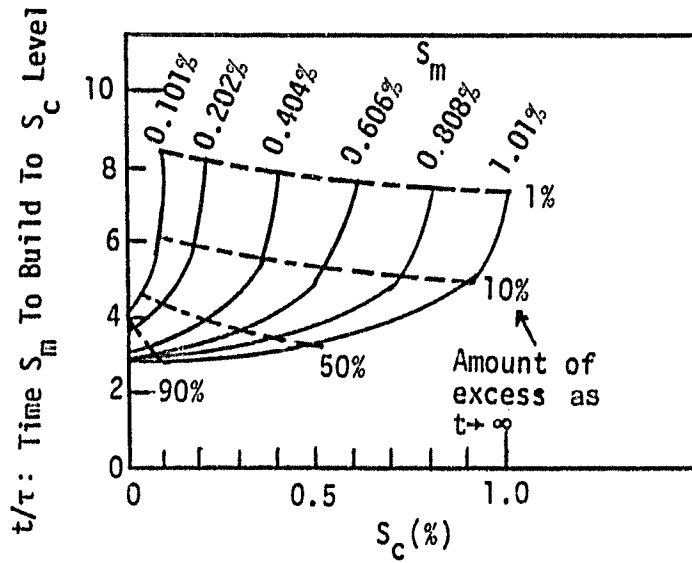
Figure 2-3. RH Transition Times for Fixed S_m

$$\frac{t}{\tau}\Big|_{S_m} = -\ln\left[\frac{(1-(1+E/100)^{-1})}{4.8495}\right] - 0.4951\ln(S_m/10)$$
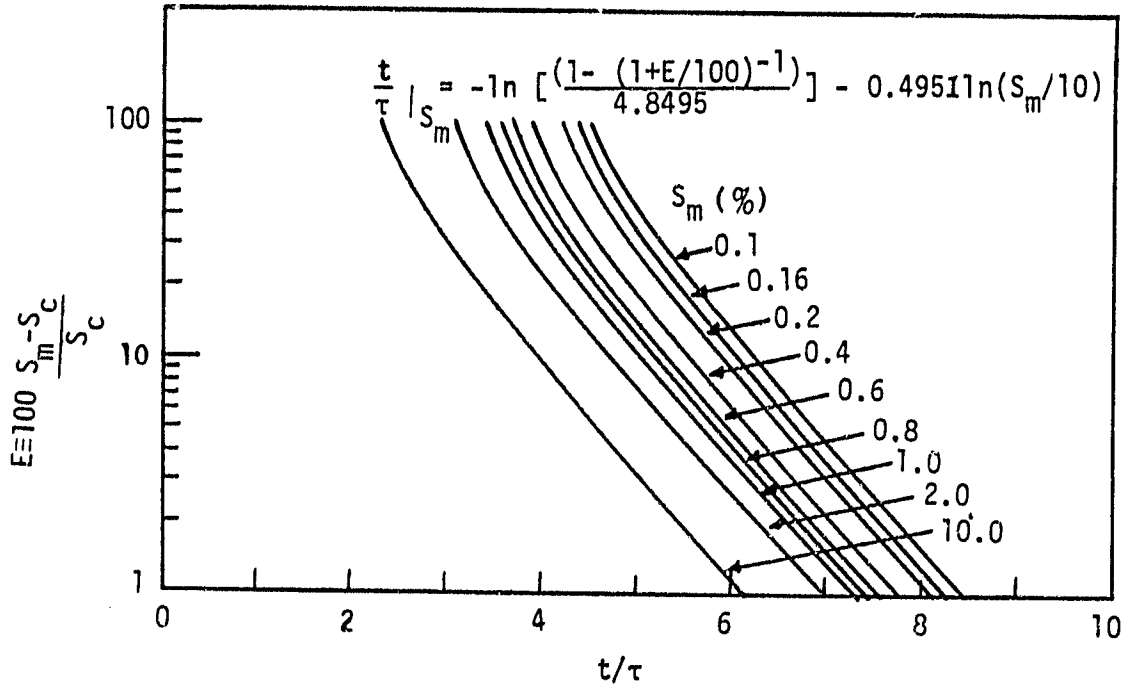
Figure 2-4. RH Transition Times as Function of Final Excess Supersaturation
Time For RH To Build From Dry/Wet Zone Value To S_c

environment or they deplete the available vapor for zero-g operation before the smaller nuclei can grow, both effects can produce errors in the chamber output count. An alternate form of Figure 2-3 is given in Figure 2-4 where the excess ,E, is plotted as a function of the number of time constants:

$$t/\tau \simeq - \ln \left[(1-(1 + E/100)^{-1})/(1 + S_0/S_F) \right]$$

Note that the curves of E versus t/τ for various S_m are parallel, hence should be collapsable onto a single curve. The equation in Figure 2-4 provides a single relationship which approximates this family of curves.

For zero-g applications, the lower S_m (< 1%) and low E (<2%) were required, hence 6.5 to 8.5 time constants would be require before these nuclei can even start growing. A significant additional time is also required to grow over the r_c region (critical radius which separates the haze and droplet regimes).

6

3.0 CHAMBER VAPOR PROFILE

As the droplets move through the CFD chamber, they may move away from the chamber centerline due to gravity, phoretic (vapor and thermal) and Brownian diffusion affects. The sample width as injected into the chamber may also extend over a finite portion of the chamber depth. In addition, the peak supersaturation is not located at the exact center of the chamber but is displaced toward the cold plate, the magnitude of the displacement being a function of the temperature difference between the plates (hence a function of S_m).

The following sections relate the peak supersaturation its location and the vapor profile to the chamber geometry and the centerline supersaturation set point S_m.

3.1 Vapor Profile About Chamber Centerline

The vapor profile between the two parallel plates in the wet/wet zone of the CFD chamber is approximately parabolic, that is the profile has a form

$$S/S_m \simeq [1 - (Z/(h/2))^2]$$

where S_m is centerline supersaturation and h is plate spacing. The supersaturation is a function of position Z where Z=0 along the chamber centerline. A log-log plot of $1-S/S_m$ versus $|Z/(h/2)|$ should give a straight line if the above relationship is true. Figure 3-1 gives profile plots for S_m = 10%, 1% and 0.1%. The heavy straight line in this figure is the true parabolic form. The actual profile above the chamber centerline (warm plate side) falls below this line and the lower (colder) portion of the profile falls above this parabolic line. As S_m approaches zero, the
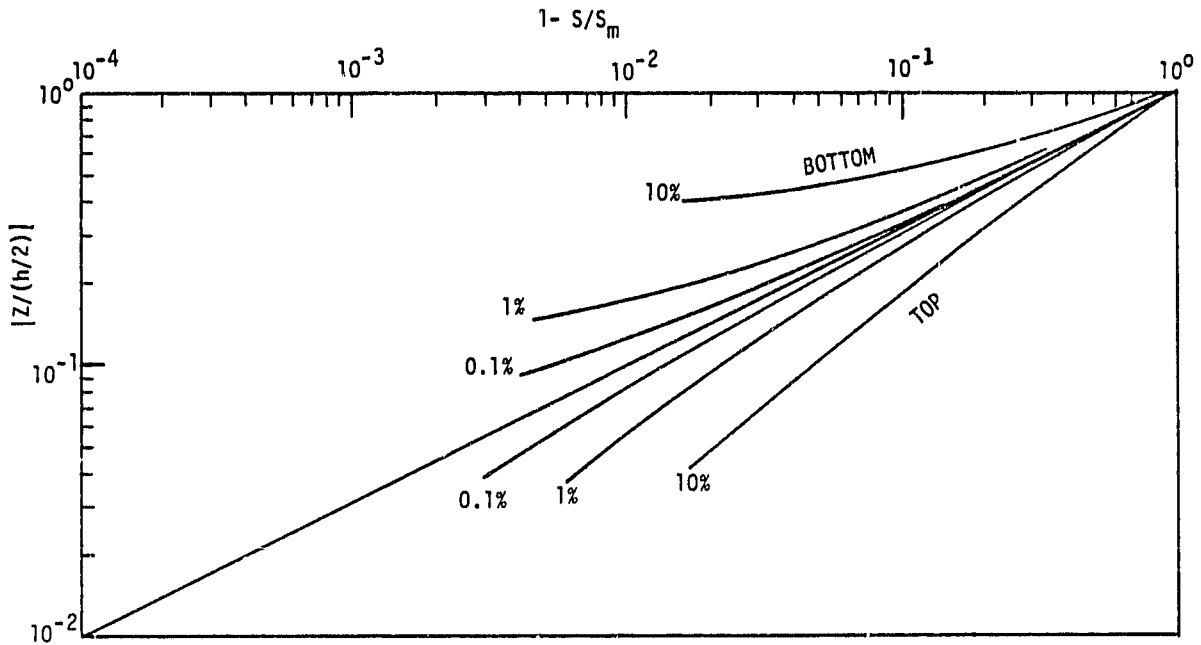
7

Figure 3-1. Wet/Wet Zone Vapor Profile About Chamber Centerline

pairs of lines approach the true parabolic form centered on the chamber centerline.

3.2 Peak Supersaturation Displacement

The position Z_o, of the peak supersaturation S_p, is known to be displaced from the chamber centerline toward the cold plate. Figure 3-2 is a plot of this displacement as obtained from the CFD simulation program. Z_o is nearly a straight line for S_p less than 1%. The simulation data provided the following approximate relationships

$$S_p \simeq S_m (1 + 0.00357 \, S_m)$$

and $\Delta Z \simeq 0.05988 \, S_m^{0.50428}$

where the values of S are in percent supersaturation.

3.3 Normalized Vapor Profile

Knowing the peak supersaturation displacement, another form for the anticipated parabolic profile can be written as:

$$S/S_m = [\, 1 - (\, (Z-Z_o)/(h/2))^2 \,]$$

where Z_o is the displacement of the parabola axis from the chamber centerline. This latter form was evaluated for the $S_m = 10\%$ data resulting in Figure 3-3. Relative to Figure 3-1, the data of Figure 3-3 falls much closer to the straight line true parabolic form. Deviations from the parabolic form occur as the chamber walls are approached, one wall now being closer to the parabola's center than the other. Values of S_m below 10% would come much closer to the true parabolic form over most of the profile. Figures 3-3 and 3-2 can be used to determine which portion of the chamber spacing that remains within specific supersaturation limits, the limits being dictated by the desired chamber activation accuracy.

9

Figure 3-2. Peak Supersaturation Displacement

The figure shows a log-log plot with $|Z_0|$ (cm) on the y-axis and $S_p (\%)$ on the x-axis, with the equations:

$$|\Delta Z| = 0.05988 \; S_m^{0.50428}$$

$$S_p \simeq S_m \; (1 + 0.00357 \; S_m)$$
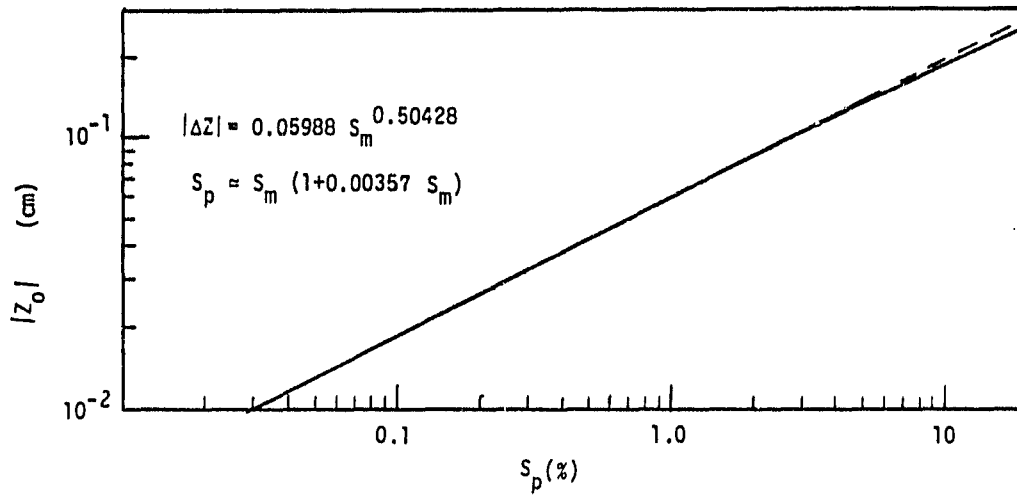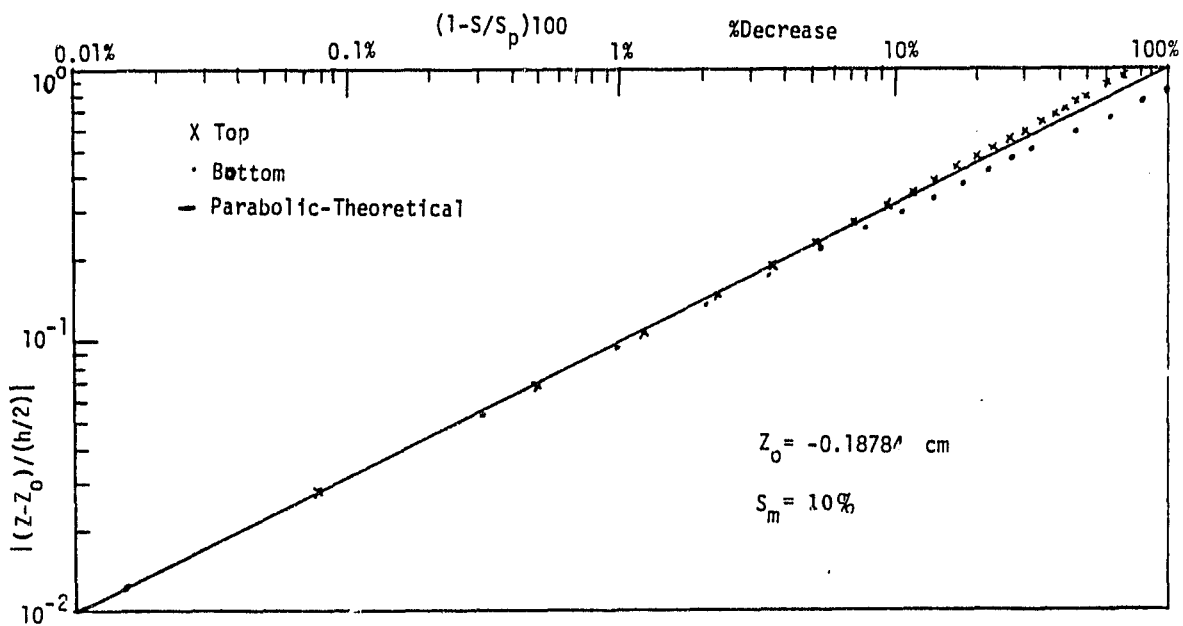
Figure 3-3. Vapor Profile about Position of Peak Supersaturation

The figure shows a plot with $(1-S/S_p)100$ %Decrease on the top axis and $|(z-z_0)/(h/2)|$ on the y-axis, with:

X Top
· Bottom
— Parabolic-Theoretical

$$Z_0 = -0.18784 \text{ cm}$$

$$S_m = 10\%$$

10

The velocity profile between the two plates is parabolic, hence follows the straight line in Figure 3-3 with S replaced by V and S_m by V_m, hence $V/V_m = (1-(Z/(h/2)^2)$.

3.4 S_m As A Function Of Chamber Temperature Difference

The wet/wet zone supersaturation profile, in particular the supersaturation along the chamber centerline, is controlled by the temperature difference , ΔT, between the two plates. The approximate relationship is ΔT kS_m. The simulation runs provided the following values of k for three chamber centerline temperatures, T_m:

T_m ($^\circ$c)	k	
	S_m = 0.2%	10%
5	18.4033	18.3700
15	21.6897	
25	25.7130	

The parameter k has slight functional dependency on S_m as illustrated above by the value of k for S_m = 10%. The above relationship is used to determine the CFD chamber plate temperature setting which will give the desired centerline supersaturation S_m.

4.0 DROPLET GROWTH TIMES

The CFD chamber geometric dimensions are governed by several factors including droplet growth time and vapor depletion. The effects of depletion were observed in the droplet growth time simulation runs and will be disussed later. The primary motivation for determining the droplet growth times was two fold: first, for a polydispersed distribution, the chamber output detector has minimum and maximum size limits within which the droplet distribution must remain to avoid count errors and second, higher experiment accuracy coupled with lower S_c values indicated that times considerably in excess of 100 seconds would be required hence having a significant impact on chamber dimensions and mode of operation. Figure 4-1 summarizes the computer runs which were performed for growth time determinations. The effects of centerline supersaturation the number of zones between the parallel plates, the nuclei flux and the plate spacing were studied.

4.1 Growth Time As Function Of Excess Supersaturation

The primary droplet growth regime of interest for the CFD chamber is from haze particles to droplets of optically detectable size (on the order of a few microns in radius). The detection lower limit is determined by the optical detector capability (approximately 0.2 microns radius) and the by size of the haze particles which exit the chamber along with activated droplets. This latter factor is a function of the dry particle radius and can extend into the micron region for critical supersaturations below a few tenths of a percent. Figures 4-2, 4-3 and 4-4 are the results of computer simulations of droplet growth within the CFD chamber where the growth time to one micron radius is plotted as a function of the excess supersaturation (S_m-S_c/S_c). Polydispersed distributions were used to provide a complete

TYPE: GROWTH TIME RUNS

T (°C)	Series (s-)	S_m (%)		Number of zones	Nuclei Flux (No./sec)	Plate Spacing (cm)	Comments
5	"Blank"	0.16	0.8	30	20	2	Depletion effects noted for excess supersatuations of 30% or less.
		0.2	1.0				
		0.4	2.0				
		0.6	10.0				
	31	0.2		10	12	4	Fewer zones and large spacing minimized phoretic effects. depletion still noticable.
	31A	0.2		10	2	2	Back to standard 2cm spacing and fewer nuclei.
	"B"	0.1	0.8	10	2	2	Still noticable depletion for excess super- s*turation of 5% or less.
		0.16	1.0				
		0.2	2.0				
		0.4	10.0				
		0.6					
	"C"	0.1	1.0	50	0.2	2	Phoretic effects only
		0.2	10.0				
15	"C"	0.1	1.0	50	0.2	2	Phoretic and mean temperature effects (no depletion)
		0.2	10.0				
25	"Blank"	0.1	0.8	30	20	2	Time and depletion effects
		0.16	1.0				
		0.2	2.0				
		0.4	10.0				
		0.6					
	"C"	0.1	1.0	50	0.2	2	Phoretic and mean temperature effects (no depletion)
		0.2	10.0				

VAPOR PROFILE - RUNS

T (°C)	Series	S_m (%)		Number of zones	Nuclei Flux (No./sec)	Plate Spacing (cm)	Comments
5		0.1		50	0.2	2	S_m effects
		1.0					
		10.0					
		1.0		30			Zones effects
15		1.0		50	0.2	2	Temperature
25		1.0		50	0.2	2	Effects

Figure 4-1.   CFD Chamber Simulation Run Summary

13

curve per computer run where the excess supersaturation range was 0.1% to 100%.

The nearly straight lines in Figures 4-2, 4-3 and 4-4 (0.2%, 1% and 10% S_m) are for growth times with no vapor depletion effects. These were obtained by keeping the nuclei concentration very low. For the remaining curves, as the nuclei concentration increases, the larger droplets (large excess supersaturation) quickly grow to several micron radii and cause localized vapor depletion hence causing extended growth times for the smaller (lower excess supersaturations) droplets which in zero-g are moving along with the larger droplets. In one-g (terrestrial laboratories) horizontal chamber operating mode, the larger droplets usually fall to the lower wall before significant depletion can take place.

The primary factor to be considered when using polydispersed aerosols is that a slight decrease in supersaturation can cause a significant increase in the growth time in the region of the droplet's critical radius in particular for the lagging smaller droplets. In this region the excess supersaturation is at its minimum, hence small changes in S_m can cause a significant percent change in $(S_m-S_c)/S_c$, the growth driving force. The result of this depletion effect is a significant increase in the droplet radii distribution width. The extended time impacts chamber dimensions and the extended radii range impacts the optical detector requirements. The more monodispersed the nuclei distribution, the more nearly the droplets grow together in size, hence minimizing the affects of this vapor depletion by the larger droplets.
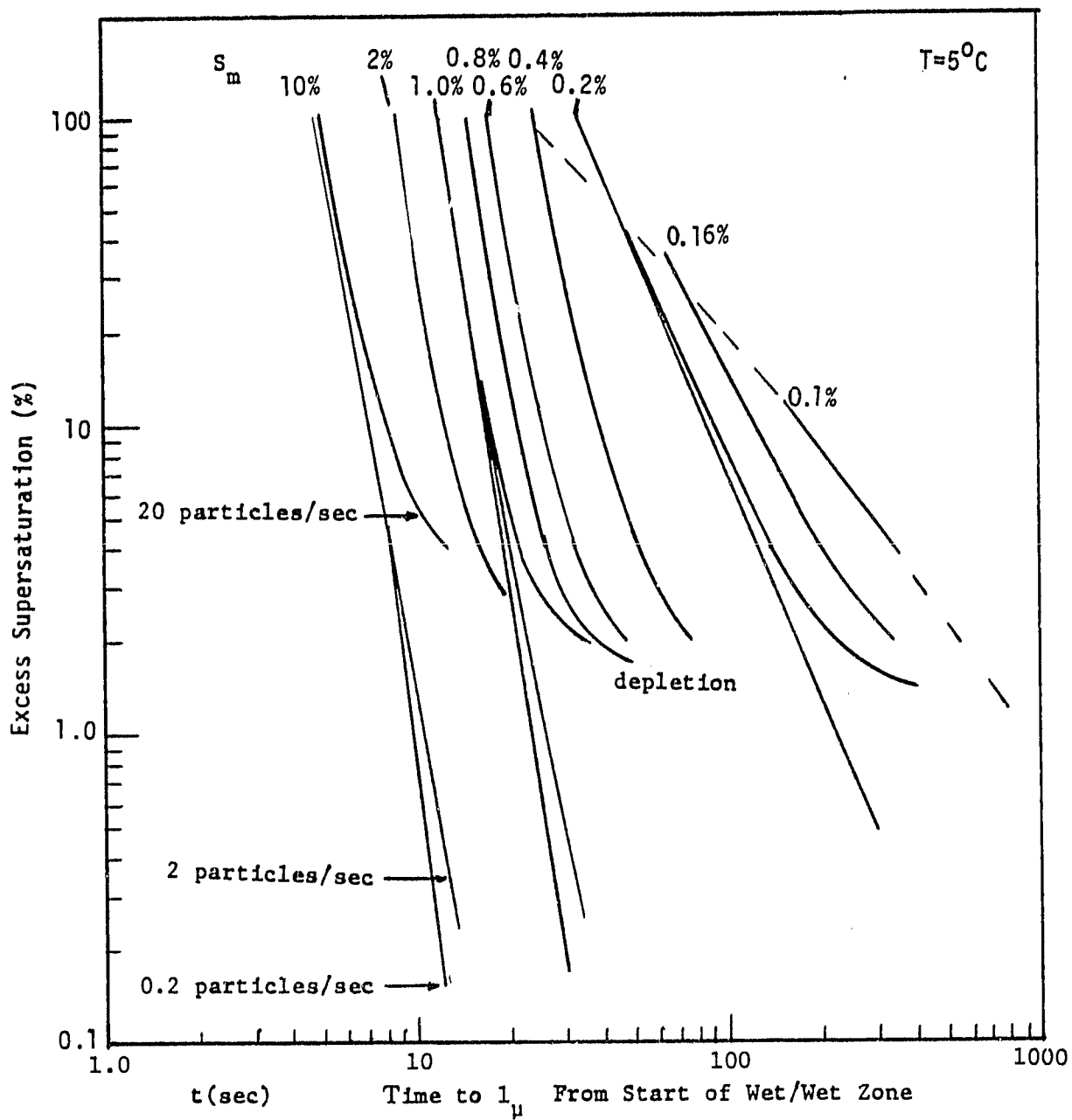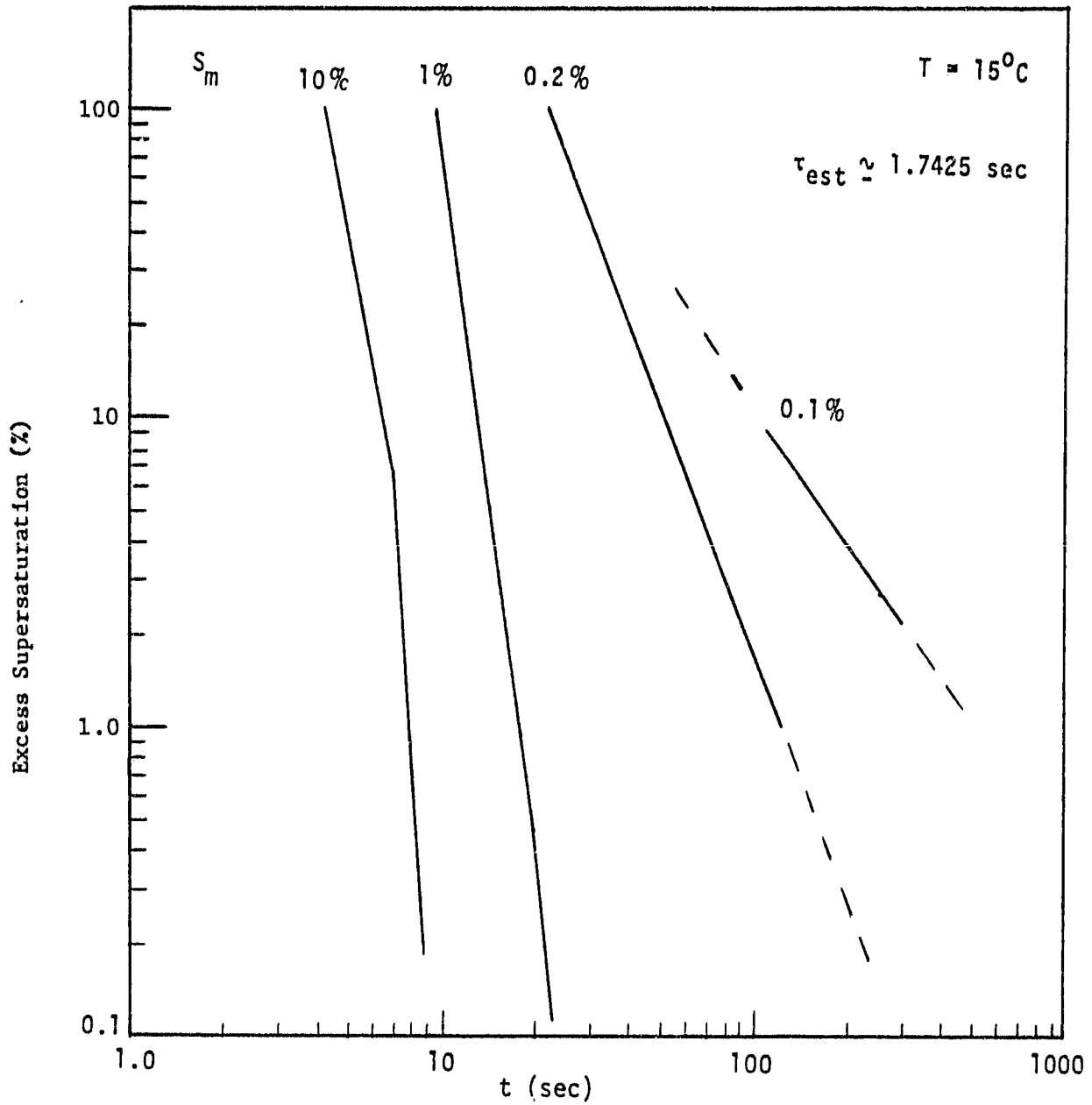
14

Figure 4-2. Droplet Growth Times - 5°C
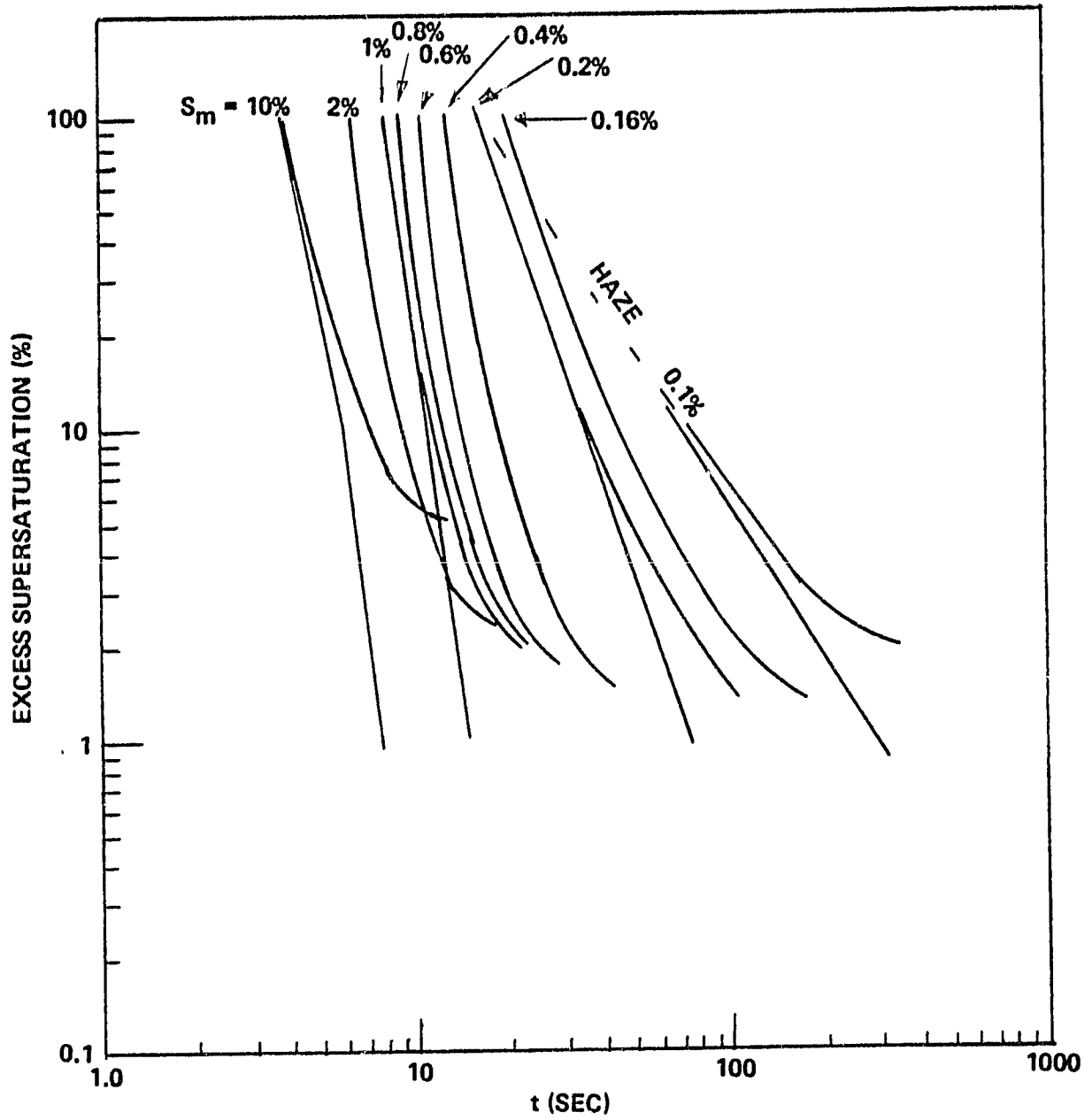
Figure 4-3. Droplet Growth Times - 15°C

Figure 4-4. Droplet Growth Times - 25°C

The families of curves (for no depletion) probably can be collapsed into a single parametric curve which would be a function of S_m, excess supersaturation and temperature. This parameterization would be useful in cloud simulation activities.

The growth time can be decreased using a lower radii limit for the sensor, perhaps 0.6 μm radius rather than the one micron used for these figures. Care must be taken that this lower detection limit does not include unactivated haze particles which would give an error in the measured aerosol size distribtuion.

4.2 Temperature Affects On Growth Time

As the temperature around the droplets decreases, the droplet growth rate also decreases, primarily due to the lower ambient vapor pressure and the lower vapor diffusivity. Figure 4-5 is a replot of the 1% and 0.2% S_m curves from Figure 4-2, 4-3 and 4-4 (5°C, 15°C, 25°C, T_m) to enhance the visualization of the affect of temperature on the time for droplet growth to one micron (no depletion effects). The combination of lower temperature and smaller S_m result in longer growth times. The added constraint of low measurement error for polydispersed nuclei distributions translates into lower permissable excess supersaturation, hence growth times in excess of a hundred seconds.

It is these lower S_m, lower temperatures and hence longer growth times which can be accommodated in a zero gravity environment. In a one-g environment, the droplets fall out of the central uniform supersaturation region of the chamber after a few tens of seconds.
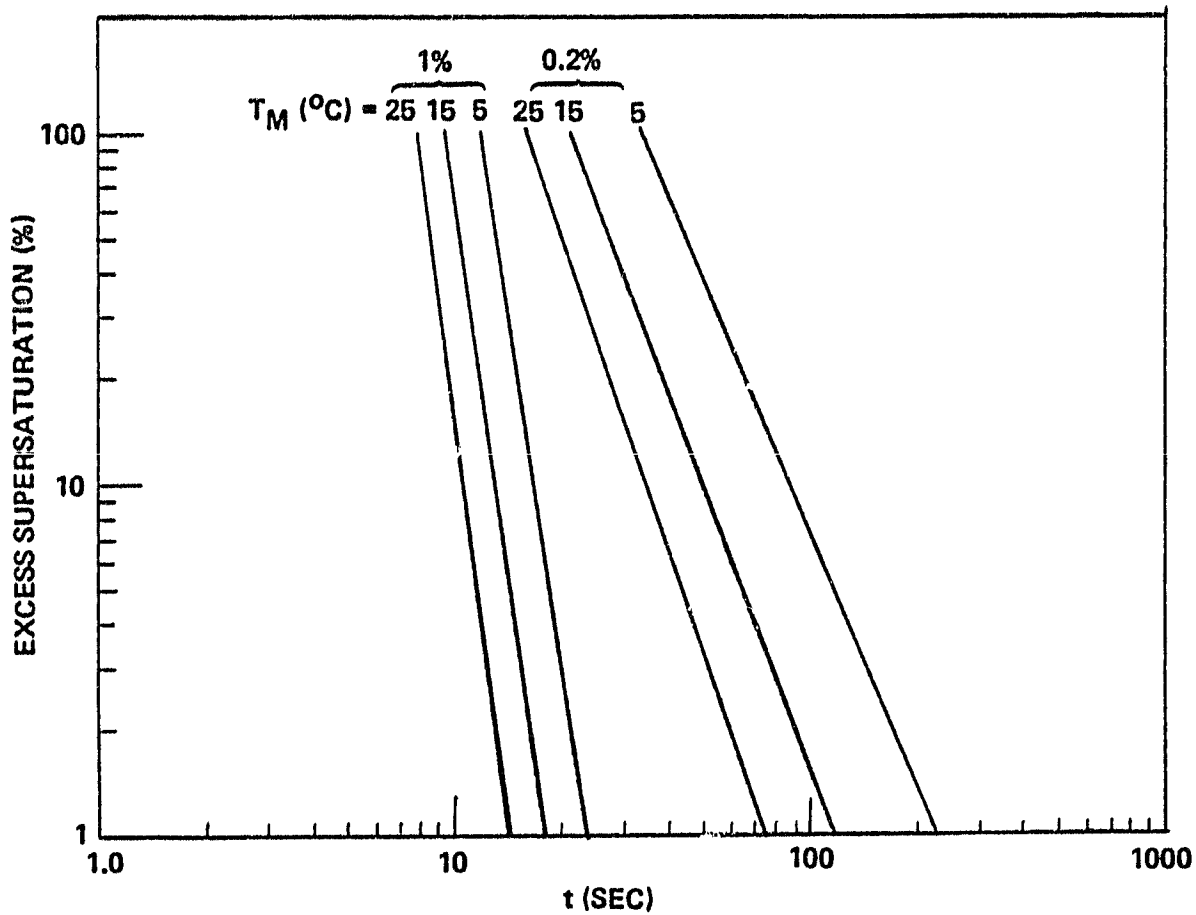
Figure 4-5. Temperature Affects on Droplet Growth Time

4.3 Growth Time Versus S_m

Another form of the data discussed in Section 4.1 is given in Figure 4-6 where the growth time to one micron is given as a function of S_m for fixed supersaturation excess. This configuration of the data again emphasises that lower S_m coupled with low excess (required for high data accuracy) leads to long growth times. A $S_m = 0.16\%$ and an excess of less than 2% results in required growth times of several hundred seconds. During this long growth time, the larger nuclei with lower S_c (higher excess supersaturation) will have grown much larger than one micron causing vapor depletion which in turn further increases the required growth time.
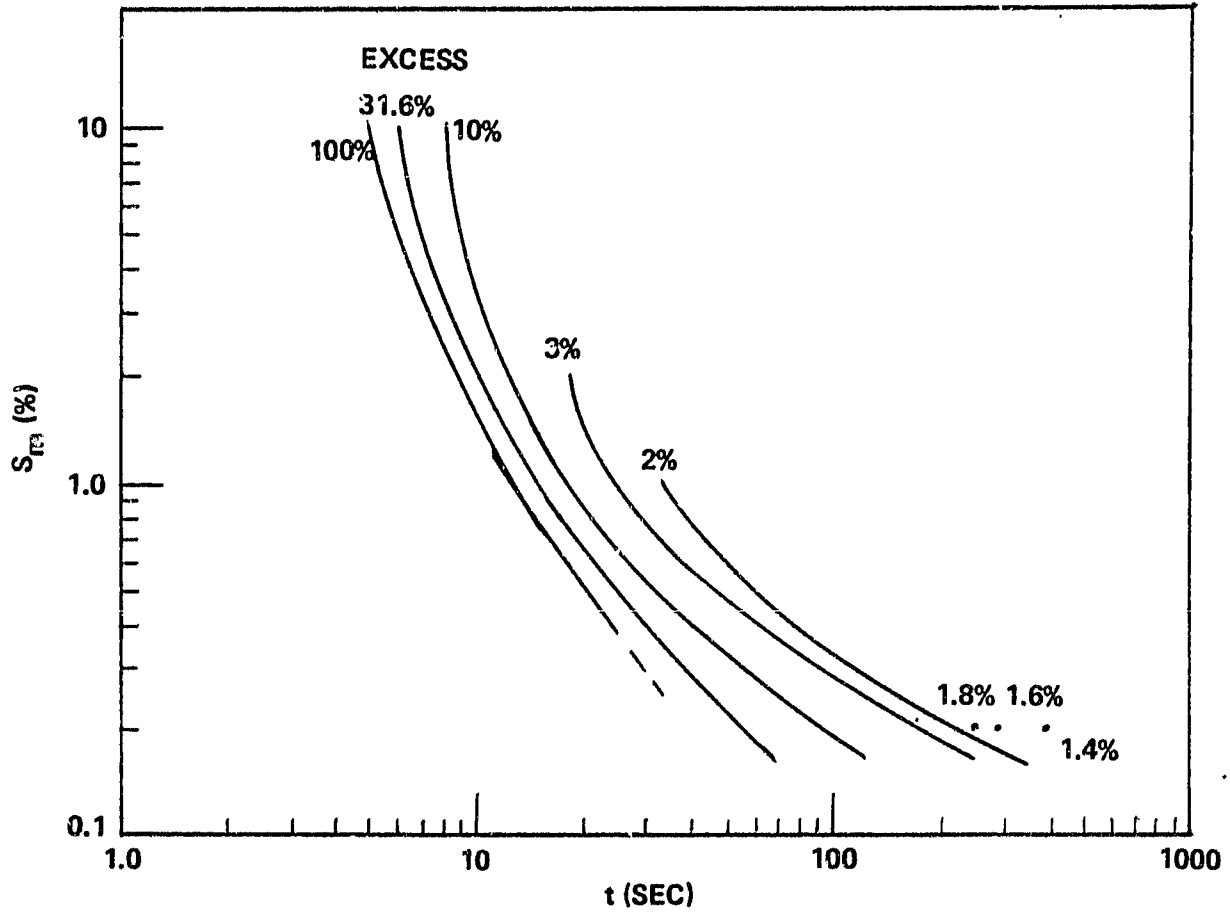
Figure 4-6. Growth Times for Fixed Excess Supersaturations

5.0 WATER VAPOR DEPLETION

With no growing droplets within the CFD chamber, a supersaturation profile will be established as discussed in Section 3. As droplets grow within the chamber, there will be a point at which the droplets will absorb the water vapor faster than the chamber walls can supply it, hence the water vapor pressure (thus, the supersaturation) will decrease. This decreased supersaturation profile manifested itself in the longer growth times as descussed in Section 4.

The evaluation of this depletion effect is necessary in order that the CFD chamber can be designed and operated within the desired error limits. The CFD model permits the numerical quantification of this water vapor depletion factor.

5.1 Monodispersed Aerosol

Hudson and Squires (1973) analytically determined the vapor depletion affects in terms of chamber and droplet parameters assuming all of the droplets were of equal radii. The decrease in the supersaturation , Δs, is given by:

$$\Delta S = 2.5 \, \sigma \, r \, S_m \, h$$

where the coefficeint 2.5 is derived from two temperature dependent terms which are practially self compensating. The radius ,r, assumes a monodispersed aerosol, S_m the centerline supersaturation, h, the plate spacing and , σ, the areal nuclei density within the chamber.

Solving for the areal density gives

$$\sigma = (2.5 \, r \, h)^{-1} \quad (\Delta S/S_m).$$

The permitted nuclei concentration is an inverse function of the droplet radius and plate spacing and is proportional to the allowable fractional depletion of the supersaturation $(\Delta S/S_m)$.

22

The permitted nuclei flux ,F, (number of nuclei/sec) is given approximately by :

$$F \simeq v \, w \, \sigma$$

where v is the centerline velocity (velocity of aerosal within the CFD chamber) and w is the sample width. The sample height is assumed to be very small relative to the plate spacing. The centerline velocity is given by:

$$v = 3 \, \dot{Q} \, / \, 2b \, h$$

where $\dot{Q}$ is the main carrier air volume flow rate (cm^3/sec) and b is the full chamber width. The flux is now given by

$$F = (3 \, \dot{Q} \, / \, 2 \, b \, h) \, w \, (2.5 \, r \, h)^{-1} \, (\Delta S/S_m)$$
$$= (3/5) \, (\dot{Q} \, / \, h^2) \, (w \, / \, b) \, (\Delta S/S_m) \, (r)^{-1}$$

For the ACPL design: $\dot{Q}$=60 cm^3/sec, b =36 cm, h= 2cm, w= 12 cm, r= 2×10^{-4}cm, the above equation gives 15 nuclei/sec for 0.1% depletion ($\Delta S/S_m$=0.001). The computer simulation run gave about 13 nuclei/sec, a value which is within about 10% of that analytically predicted.

5.2 Polydispersed Aerosol

Most aerosols that are measured with the CFD chamber are not truly monodispersed (single radii) but have a range of radii, i.e., polydispersed. The total depletion , σ_τ , due to a range of droplet sizes can be expressed as a sum over the depletion due to each size , σ_i, hence:

$$\Delta S_T = \Sigma \Delta S_i = 2.5 \, h \, (\Sigma \sigma_i \, r_i) \, S_m$$

If each droplet size ,r_i, has f_i, fraction of the total areal concentration such that $\Sigma f_i = 1$, then:

$$\Delta S_T = 2.5 \, h \, S_m \, \sigma_\tau \, \Sigma \, f_i \, r_i.$$

Solving for the areal concentration

$$\sigma_T = (2.5 \, h)^{-1} \, (\Delta S_T/S_m) \, (\Sigma \, f_i \, r_i)^{-1}$$

and the flux for a polydispersed distribution is given by an expression similar to that in Section 5.1, that is:

$$F = (3/5) \quad (\dot{Q} / h^2) \quad (w / b) \quad (\Delta S/S_m) \quad (\Sigma f_i \, r_i)^{-1}$$
$$= (3/5) \quad (w / b \, h^2) \quad \dot{Q} \quad (\Delta S/S_m) \quad (r_{eff})^{-1}$$

where r has been replaced by $\Sigma f_i \, r_i$, a sum over the size distribution. Hence this sum can be thought of as an effective radii ,r_{eff}, which causes the equivalent vapor depletion. The first term is a scale factor and has some temperature dependency. The second term (3/5) above contains CFD chamber geometric factors which coupled with $\dot{Q}$ determines the aerosol/droplet residence time in the chamber and $\Delta S/S_m$ is the tolerable depletion factor.

The effective radii ,r_{eff}, for various polydispersed activated droplet distributions are summarized in Figure 5-1. The effective dispersion width is assumed to be:

$$\Delta r = r_{max} - r_{min} = M \, r_{min} - r_{min} = r_{min} \, (M-1)$$

where the multiplier M relates maximum droplet size (radius at which 99% of the droplets radii are less than) to the minimum size. Several curves are given for which 99% of the droplet radii are greater than r_{min}. Hence an M equal to one and r_{min} = 1 micron is for a monodispersed distribution with all radii at one micron and with M equal to 10, 98% of the radii are between 1 and 10 microns. The r_{eff} versus M (distribution width) curves are approximately linear (c.f., Figure 5-1). Since the allowable flux of droplets is inversly proportional to r_{eff}, a droplet distribution width of M=10 will reduce the allowable flux by a factor of about 3.5 below the permitted flux for a monodispersed distribution (i.e., M=1).
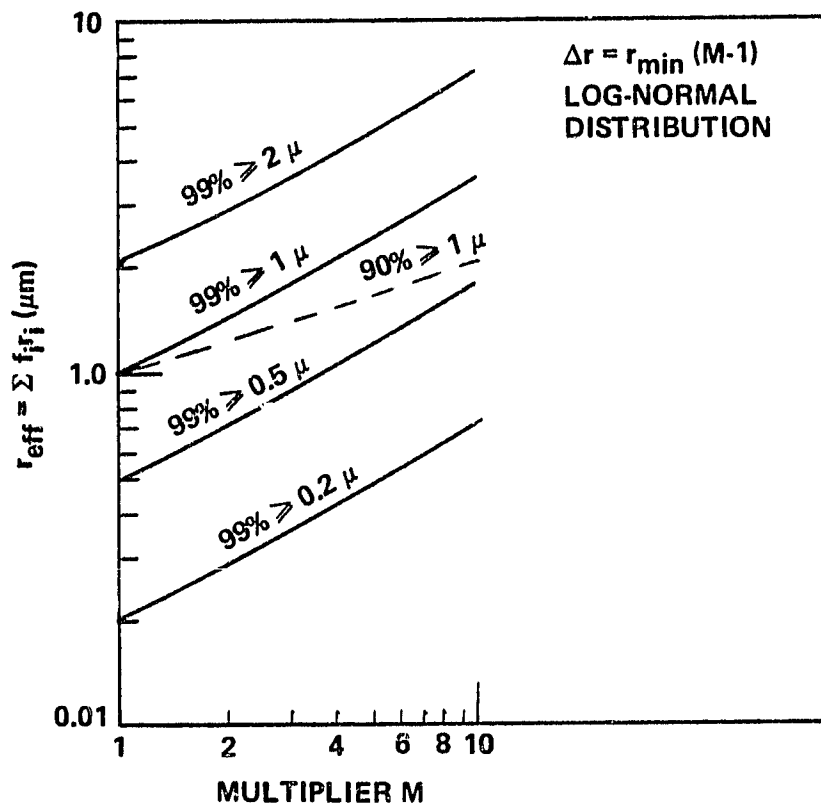
24

Figure 5-1.   Effective Radii for Polydispersed
              Droplet Distributions

These r_{eff} curves (for a fixed M, distribution width) scale proportional to r_{min} as also shown in Figure 5-1 for r_{min} = 0.2, 0.5, 1 and 2 microns. The permitted flux of droplets through the CFD chamber for a given depletion factor is invesely proportional to this r_{min}.

The affect of permitting larger error in the final count, for example, only 90% of the droplets are between the detectable limits of r_{min} and Mr_{min}, results in a decrease in r_{eff} as shown by the dashed line for r_{min} = 1 micron. The allowable flux for a 10% error in count (i.e., 90% of radii between detector limits) and for a distribution with M=10 is about 50% of that for a monodispersed distribution (M=1).

A comparison of r_{eff} with d*(class with most particles) showed that r_{eff} goes up a little more rapidly the d*, that is, the larger droplets have more influence on the depletion (as would be expected). The area related diameter ,d_a, goes up too rapidly. The log-normal distribution characteristic diameter which most closely tracks the affects on depletion of the distribution width is dg (the geometric mean). Thus changes in the dg for the activated aerosol (note that this d_g is for the activated droplets, not the original aerosol) can be used to assess expected changes on the CFD chamber vapor depletion, hence the affects on chamber detection error.

5.3 Characteristics of Polydispersed Log Normal Distributions

A log-normal distribution can be characterized by the standard deviation σ_g and the radius r_g (geometric mean radius). Figure 5-2 graphically shows curves with different values of sigma. The distributions
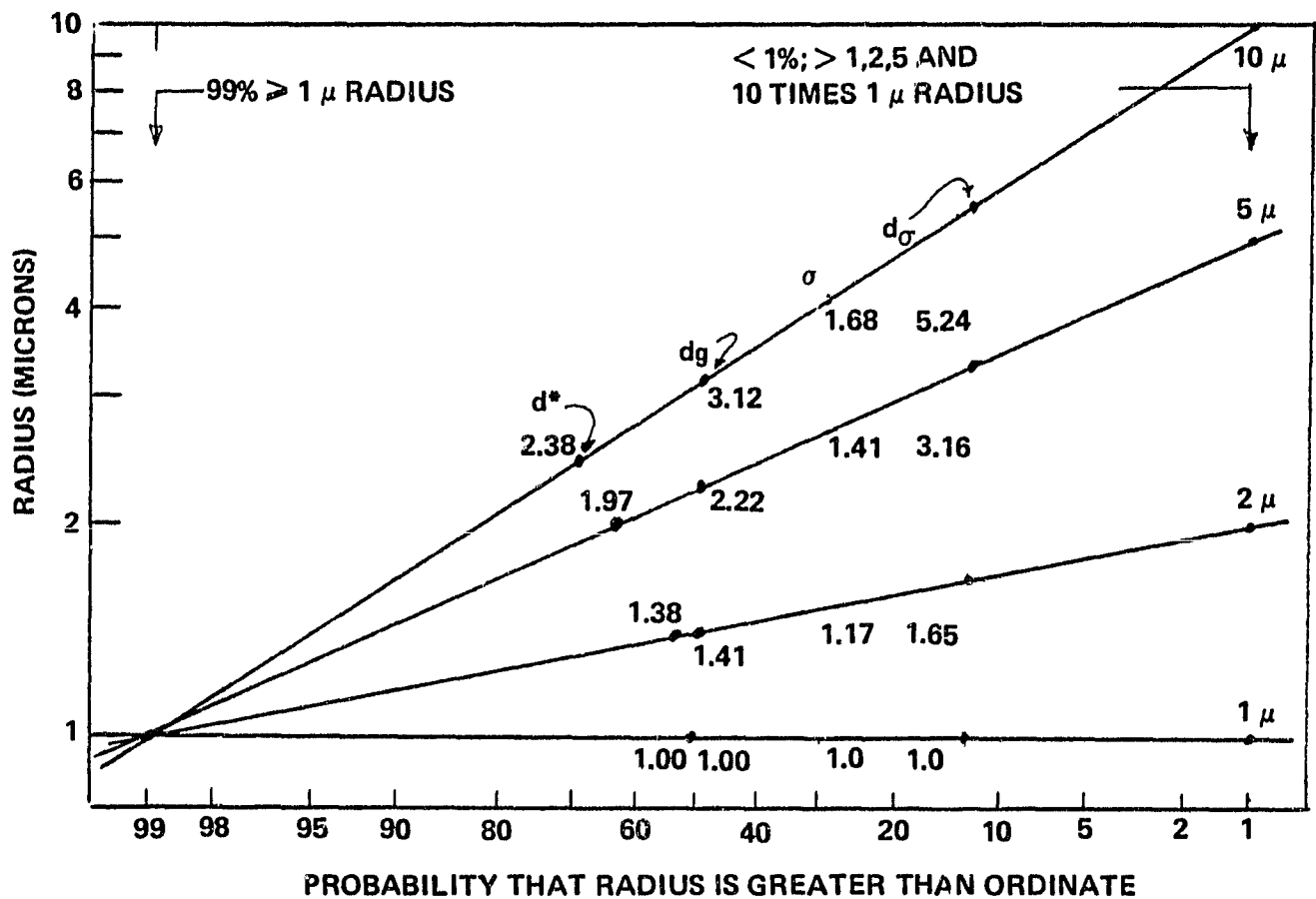
26

Figure 5-2.   Log-Normal Droplet Distributions

were all assumed to have 99% of the droplet radii greater than or equal to one micron with less than 1% greater than 1, 2, 5 and 10 microns.

5.4 Spread in Final Radii Distribution

A summary of the final radii distribution as a function of the initial nuclei distribution width is given in Figure 5-3. No depletion occurred. A spread in the radii above about one micron radius is primarily due to the slow growth rate of the droplets as their radii move across the critical radius r_c (the radius separating haze regime from growing droplet regime). As the excess supersaturation increases, the spread in droplet radii for a fixed initial distribution decreases. As the minimum detectable radius increases, the distribution becomes narrower in terms or r_{max}/r_{min}. As the pemitted count error decreases, the excess supersaturation for the higher S_c classes decreases and the width of the output droplet distribution becomes larger.
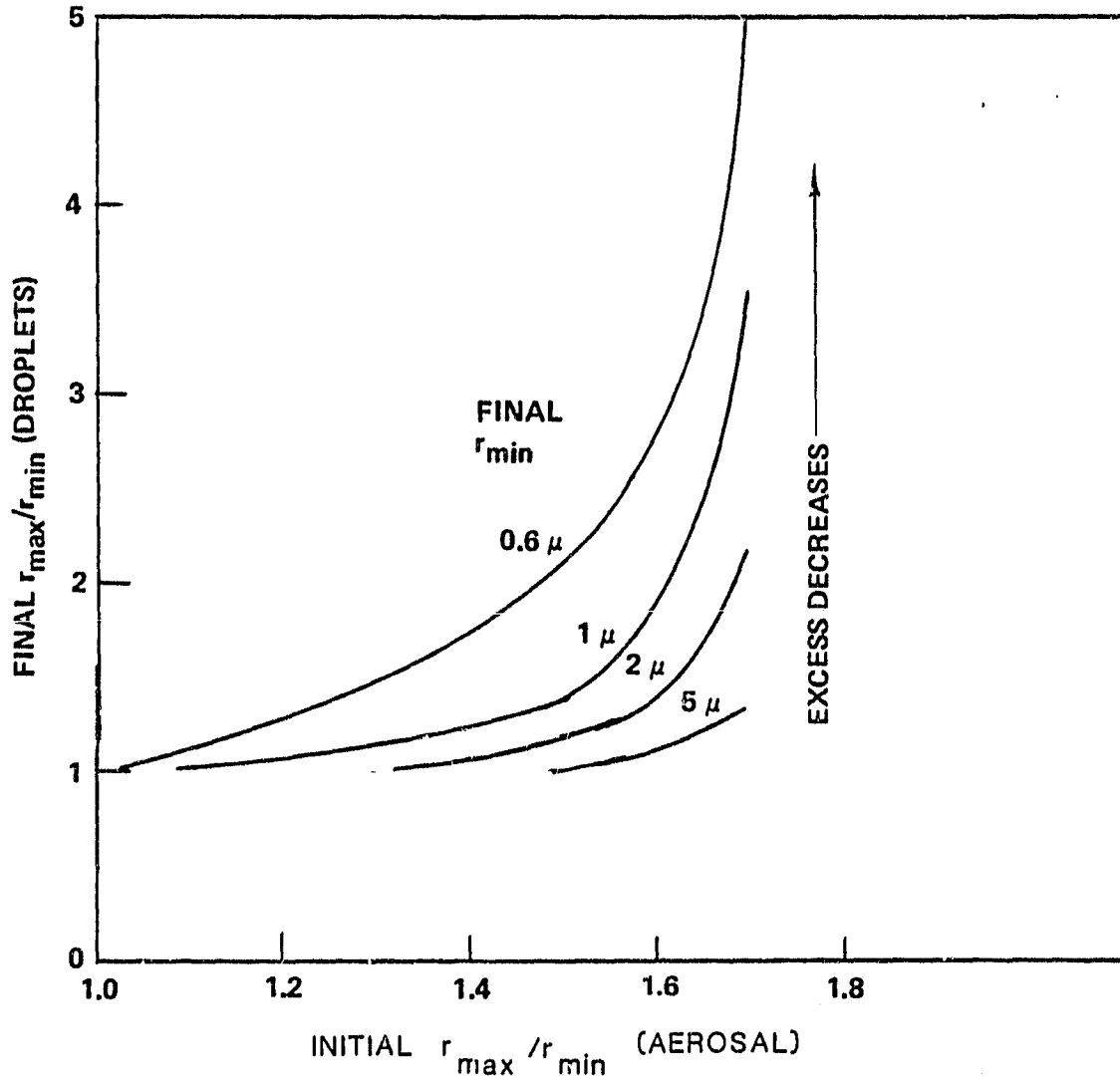
Figure 5-3. Spread in Final Radii Distribution as Function of
Initial Nuclei Distribution

6.0 ONE-G CFD CHAMBER OPERATION

A number of one-g simulation runs for the CFD chamber in a horizontal mode were performed and the data reported in Neste and Eaton (1981). More runs were performed during the latter part of this contract but a full assessment of them were not performed due to limited time. Some general conclusions can be drawn for the one-g, horizontal mode of operation. Optimum operating conditions include:

a) Operation at lower temperatures (10 to 15°C) slows the droplet growth rate down permitting more precise control and measurement of chamber parameters.

b) A narrower aerosol distribution (preferably monodispersed) minimizes the fall out of the larger droplets prior to the growth of the smaller droplets to detectable radii.

c) A low areal aerosol concentration within the CFD chamber is very important when errors of less than 10% are being sought.

d) The detector threshold should be set as low as possible to count the droplets prior to gravity induced fall out. An optical detector with more than fifty logarithmic spaced channels extending down to 0.2 micron radius would be good with post experiment determination of the usable threshold setting. Care must be taken that the selected threshold is above any haze droplet that are with the activated droplets.

e) Lower S_c also enhances the horizontal, one-g operation mode.

An estimate for the permisable polydispersity in a one-g environment is given in the next section.

6.1 One-G Supersaturation Range

In one-g as described earlier, the droplets can fall to the the lower plate if they remain in the CFD chamber for too long of a time when operated in an horizontal mode. The problem of fall out can not be circumvented if the nuclei distribution width is restricted between certain limits. An

estimate of the allowable critical supersaturation range for one-g can be expressed in terms of a range of allowable excess supersaturation range. Aerosol critical supersaturations above the range will take too long to grow and be undetected while those below this range will grow too fast and fall to the lower plate before exiting the chamber. The data plotted in Figure 6-1 is for $5^{\circ}C$, $S_m = 0.2\%$ and a plate spacing of two centimeters. The left curves for 0.6 microns and 1 micron are for the minimum size countable as determined by the threshold setting selected for the droplet detector. The right hand curve is the distance travelled (hence time) in the wet/wet zone until either the droplet fell to the bottom plate or the droplet evaporated back to 0.6 microns or less due to its motion into the lower supersaturation portions of the water vapor profile near the lower plate (no depletion effects). The dashed lines in Figure 6-1 illustrates an example for determining the permissible (detectable) range of excess supersaturations. Assuming a lower detecton limit of 4% excess and a detection threshold of 0.6 microns, the upper limit (following dashed line) set by droplet evaporation or fall out is about 13% excess supersaturation. The S_m for this run was 0.2%, hence the range of S_c permitted will not exceed the range of 0.177% to 0.192%.

This excess supersaturation range as a function of the desired lower detectable excess (as determined by error considerations) is plotted in Figure 6-2 as obtained from Figure 6-1. The higher the threshold excess supersaturation, the broader the detectable critical supersaturation range and hence the broader the nuclei radius distribution. This is a result of S_m moving upward away from the larger S_c being detected, hence excluding the droplets which grow slowly through the r_c regime. As higher experiment precision is demanded, the narrower the allowable nuclei radius distribution
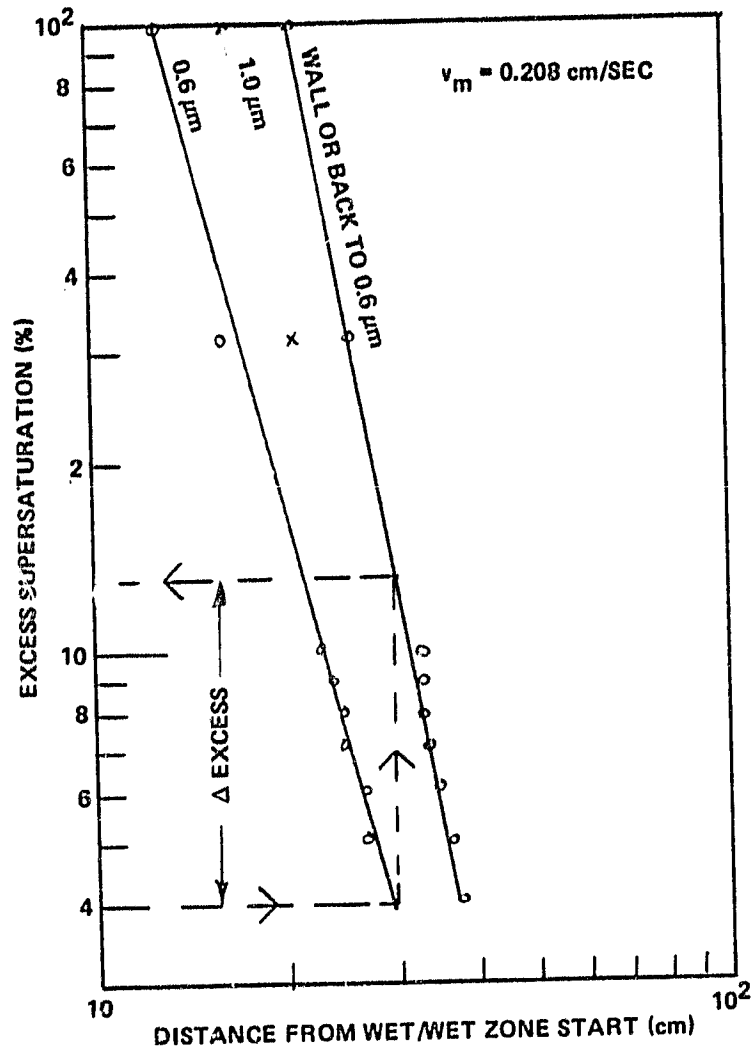
31

Figure 6-1. One-g Growth Distance (Time) Range as
Function of Excess Supersaturation

32

must be for a one-g horizontal operating mode (this also applies to the SDL chamber). Thus a minodispersed aerosol distribution would be best for one-g chamber calibration.

In zero-g a larger nuclei radius range is permitted but the depletion caused by the larger droplets then becomes the operational limit on the permissable size distribution width.
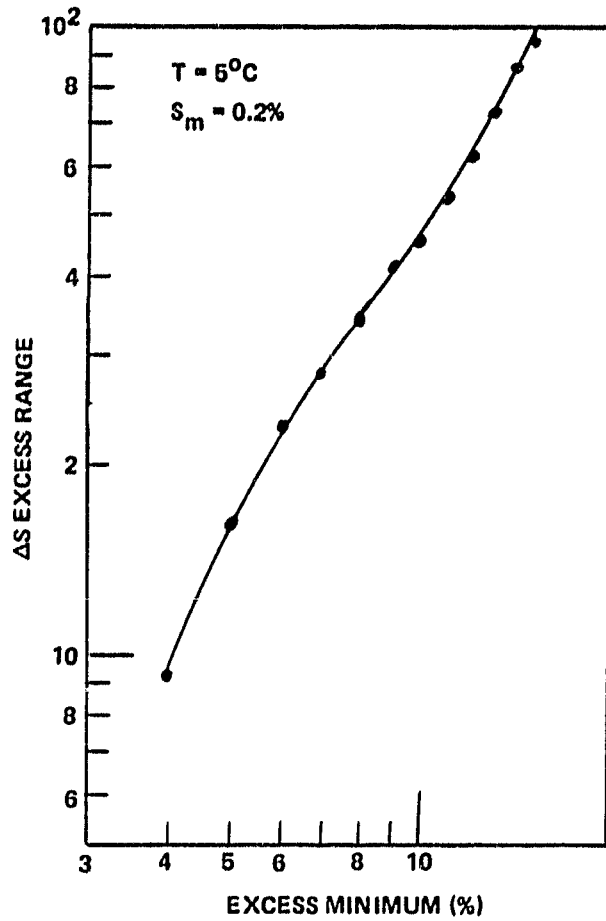
Figure 6-2. Allowablᵉ Excess Supersaturation
Range for One-g Horizontal CFD
Chamber Mcᵈe

7.0 SUMMARY

The vapor profile in the wet/wet zone of the CFD chamber is nearly parabolic with the origin of the parabola displaced from the chamber centerline, the displacement being a function of the centerline supersaturation setting. A single parametric equation is derived for this profile.

Droplet growth time in the CFD chamber can extend to hundreds of seconds for smaller S_c and lower experiment error (<3%). Vapor depletion affects of a polydispersed distribution can be characterized by an equivalent single droplet radius.

There are several operating conditions which can be used to optimize the operation of the CFD chamber in a one-g horizontal mode. Although the horizontal mode can not provide the droplet growth times of the vertical mode of opeation, it can provide a very precise method for checking aerosol nucleation theory over a limited S_c range.

When high precision data (error significantly less than 10%) is desired in zero-g from the CFD chamber there are several areas which must be carefully assessed. Higher precision requires that the nuclei with critical supersaturations ,S_c, near the chambers peak supersaturation ,S_p, be given sufficient time to grow. As S_c approaches S_p, much more time is required to grow through the corresponding critical radius, r_c region. Over 50% of the total growth time to one micron can be expended in the radius regime of $r_c \pm$ 10% r_c. The assumption that the droplets have grown beyond r_c by the time they have moved seven vapor diffussion time constants into the wet/wet zone is not true when high precision is required.

$C - 2$

35

A spread in nuclei sizes (polydispersed distribution) can cause water vapor depletion problems in a zero-g environment which further increases the required growth time. In one-g, the larger droplets fall out thus diminishing the depletion problem but cause count errors due to loss of droplets.

Aerosol sample width within the chamber becomes very restricted as the precision requirements increase. As droplets move out of the peak supersaturation region, longer growth times are required: some droplets may not be activated that should have been.

8.0 REFERENCES

Neste, S. L., and 1. R. Eaton: Phoretic Motion Experiment-Final Report.
NASA/MSFC contract number NAS 8-33149. September 1981.

Hudson, J. G. and P. Squires: Evaluation of a continuous cloud nucleus
counter. J. Applied Meteorology, 12, 175-183. February 1973.